ALMA MATER STUDIORUM · UNIVERSITY OF BOLOGNA

School of Science
Department of Physics and Astronomy
Master Degree in Physics

Timing resolution studies of irradiated SiPMs for the ALICE 3 experiment

Supervisor:
Prof. Gilda Scioli

Co-supervisor:
Dr. Bianca Sabiu

Submitted by:
Michele Maestrelli

Academic Year 2023/2024

Abstract

ALICE 3 is a next-generation multipurpose detector, designed as an upgrade of the present ALICE experiment for the LHC Runs 5-6. To enable the physics programme which aims at studying the properties of Quark-Gluon Plasma, ALICE 3 features high readout rate capabilities, superb pointing resolution and excellent tracking and particle identification over a large acceptance. One of the main requirements for the PID system is a Time-Of-Flight (TOF) detector for time measurements with 20 ps resolution. Silicon PhotoMultipliers (SiPMs) are among the possible candidates for the outer layer of the TOF detector, due to their high efficiency and their capability to directly detect charged particles thanks to the Cherenkov light produced through the standard protection layer of the SiPM. SiPMs of 1×1 mm^2 area with 1 mm and 1.5 mm silicone protection were studied in this context to evaluate their performance before and after irradiation: indeed, their performances were previously studied in beam test at CERN-PS and after being irradiated with 10^9 and 10^{10} MeV $\mathrm{n_{eq}}$ cm^{-2} it is shown that, thanks to the very high signal detected on the SiPM at the passage of a charged particle, the sensors maintain an excellent time response. Even if DCR gets higher with respect to new SiPMs, a high noise rejection can be obtained once an appropriate threshold is applied to the signal. These studies on the possibility to use SiPMs as particle detectors are crucial for their possible future applications in many areas.

Contents

Introduction

ALICE (A Large Ion Collider Experiment) is an experiment at the Large Hadron Collider (LHC) with the aim of studying heavy-ions collisions in order to investigates the properties of the Quark-Gluon Plasma (QGP). A compact next-generation multipurpose detector named ALICE 3 is proposed for LHC Run 5, around 2033, to be located where the ALICE experiment is currently installed. The timing layers of ALICE 3 require the stringent time resolution of 20 ps in order to be able to do Particle IDentification (PID) and enable the ALICE 3 extensive physics programme. With this time resolution PID, the discrimination of pi/k/p could be up to 2 GeV/c and hadrons/electrons up to 500 Mev/c. This goal could be achieved with a Time-of-Flight (TOF) silicon based detector system composed of an inner layer, an outer layer and forward disks. The R&D is conducted considering as baseline candidates for the inner layer of the TOF fully-depleted Complementary Metal-Oxide-Silicon (CMOS) Monolithic Active Pixel Sensors (MAPS), and as backup solution Low Gain Avalanche Detectors (LGAD) and Silicon Photomultipliers (SIPMs). Due to SiPMs limits in radiation hardness, these detectors are under study for the outer TOF layer.

SiPMs are solid-state detectors made of an array of hundreds or thousands of integrated Single-Photon Avalanche Diodes (SPADs) operating in Geiger mode. With respect to traditional photodetectors such as photomultiplier tubes (PMTs) they can operate at low voltages (typically 20-70 V), they can detect very low light level across a broad spectrum (near UV to visible light), they are compact and insensitive to the presence of a magnetic field. This makes them suitable for a variety of applications, not only in High Energy Physics (HEP) but also in medical and astrophysical fields. In [1, 2] it was quantitatively shown that charged particles can be directly detected with SiPMs thanks to the Cherenkov radiation produced at the passage of the particle through the standard protection layer placed on top of the SiPM. A very high number of firing SPADs was observed with a time resolution around 20 ps for events with more than 5 firing SPADs, which constitute the majority of the statistics..

In the context of ALICE 3 R&D, the ALICE group of INFN-Bologna conducts every year a series of beam tests at CERN-PS T10 beamline facility in order to test different samples of silicon sensors with the aim of study their time resolution. In this thesis work, two samples of SiPMs are considered. They are NUV-UV-RH (Near UV - High Density-Radiation Hard) devices developed by Fondazione Bruno Kessler (FBK) of 1×1 mm^2 active area covered by a protection layer of resin of 1.0 mm and 1.5 mm thickness. These sensors have been studied for the first time in a beam test at CERN in November 2022 and then have been brought to TIFPA (Trento Institute for Fundamental Physics and Applications) in Trento for a radiation campaign in which they have been irradiated with a dose of 10^9 and 10^{10} MeV n_{eq} cm^{-2}, based on the sample. Then, they have been tested again at CERN during a beam test in July 2023. In this thesis, their performances in terms of noise and time response of the SiPMs are compared before and after being irradiated.

In Chapter 1, the main physics goals of ALICE experiment are shown together with an overview of the future ALICE 3 detector, with a particular attention to the timing layers and the main sensor technologies involved.
In Chapter 2, the physics of the solid state detector is introduced focusing on the particle interaction with a silicon detector and the working principle of the SiPM.
In Chapter 3, experimental results conducts on two NUV-HD-RH SiPMs 1×1 mm^2 are shown, on the basis of the data collected at CERN-PS T10 beamline during November 2022 and July 2023 beam tests. The performances of the two sensors are compared before and after the irradiation campaign.

Chapter 1

ALICE 3: A next-generation heavy-ion experiment at the LHC

ALICE (A Large Ion Collider Experiment) is an experiment at the LHC (Large Hadron Collider) with the aim of studying heavy-ions collisions in order to determine the properties of strongly interacting matter at extreme densities and temperatures, similar to those found a few microseconds after the Big Bang, i.e. the so called Quark-Gluon Plasma (QGP) phase.

During LHC Run 1 (2009-2013) and Run 2 (2015-2018) crucial results were obtained in understanding the properties of the QGP, thanks to very precise measurements of the total yields of different particle species. Investigation in the heavy-flavour sector and of the charmonium state J/ψ production allowed to figuring out a new production mechanism by combination of deconfined charm and anti-charm quarks. However, a precise description of partons hydrodynamization and thermalization in dense QCD (Quantum ChromoDynamic) matter has not been provided yet. In addition, the hadronisation mechanisms in the heavy flavors sector is not fully understood.
The main goal of ALICE during Run 3 (2022-2025) and Run 4 (2029-2032), where the integrated luminosity for Pb-Pb collisions will approach ~ 13 nb^{-1}, consists of precise measurements of heavy flavor production and of baryon to meson ratios. For instance, the measurements of the D_S^+ and Λ_C^+ yields over a broad p_T range and elliptic flow will be fundamental in order to better understanding and giving constraints to the hadronisation mechanism via recombination. The program of Runs 3 and 4 contains also the first measurement of thermal dilepton production with the aim of determine the temperature interval reached in the early phase of the collisions, before the hadronisation phase. Such measurements will be fundamental also to investigate the chiral symmetry restoration mechanism at high temperature.

The rich scientific program presented so far is nevertheless affected by the experimental limits of the present ALICE detector. New sub-detectors will be installed before

Run 4, like the new Inner Tracking System (ITS 3) and the Muon Forward Tracker, both based on Monolithic Active Pixel Sensors (MAPS), while the installation of a major upgrade of the whole apparatus, named ALICE 3, has been scheduled for LHC LS4 (Long Shutdown 4) (Fig. 1.1) at the LHC Interaction Point 2, where the present ALICE experiment is installed. The proposed detector is conceived for studies of pp, pA and AA collisions at luminosities a factor of 20 to 50 times higher than the ones reached with ALICE upgrades with the upgraded ALICE detector. ALICE 3 will be a silicon-based detector with an extremely material budget, excellent tracking and vertexing capabilities, to cover a wide p_T range down to few tens of MeV/c: in particular, the Particle IDentification (PID) will be realised via a Time of Flight (TOF) detector whose target time resolution is of the order of $\simeq$ 20 ps.

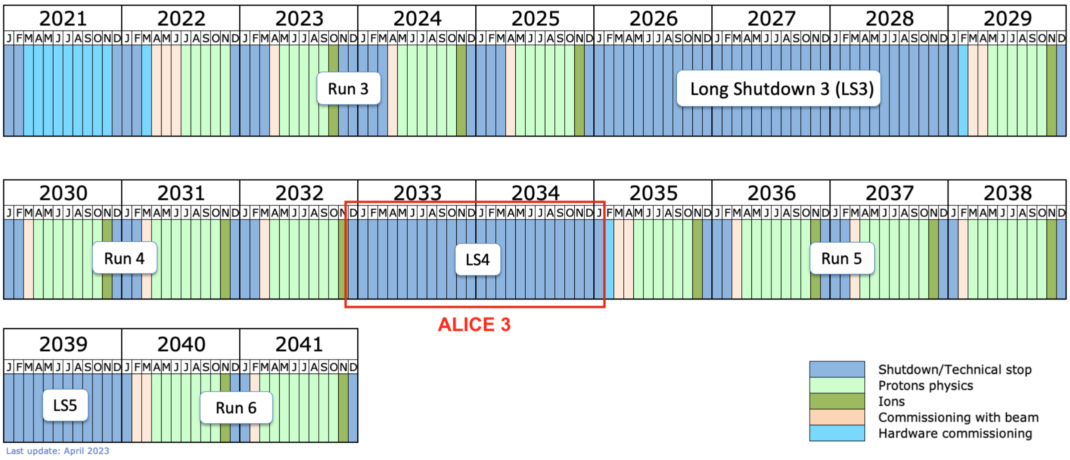

Figure 1.1: Long term LHC schedule. ALICE 3 is planned to be installed during LS4. From [3].

Within the prospective to investigate multi-charm baryons, some states such as Ξ_{cc} and Ω_{cc} will be accessed via a remarkable tracking resolution of the order of few micrometers. In the quarkonium sector, for the first time the measurements of high precision ratio of ψ(2S) and J/ψ at central rapidity will be crucial for strongly discriminate the different models of charmonium formation from deconfined $c\bar{c}$. The large pp and p-Pb samples will allow to give a description of the production mechanisms of hypernuclei, by extending the measurement of hyperon-hyperon interaction.

1.1 QGP from heavy-ion collisions

Quantum Chromodynamics (QCD) is the gauge field theory describing the strong interaction. QCD is based on a non-abelian symmetry group SU$(3)_C$ and its Lagrangian is local invariant under transformations of SU$(3)_C$. Two processes can be distinguished:

1. large momentum transfer processes, corresponding to a small value of the strong coupling constant α_S. This is the condition where *asymptotic freedom* is observed and it can be studied with a perturbative approach (pQCD);
2. low momentum transfer processes, corresponding to large values of α_S, require a non-perturbative approach. This is the condition where *confinement* is observed, chiral symmetry is spontaneously broken and only composite objects, hadrons, can be detected. A theoretical description of this regime is the lattice QCD (lQCD).

Heating a system of quarks and gluons at large energy density up to a temperature exceeding 150-160 MeV and compressing it at high pressures, leads to the creation of the QGP. The QGP corresponds to a QCD phase transition from confined matter to a deconfined state of colored quarks and gluons, where the chiral symmetry breaking is no longer present. Two fundamental parameters are the bariochemical potential μ_B and the pseudocritical temperature. The first represent the energy required to add or remove a baryon from the medium: for low values of μ_B, associated to high-energy collisions, the transition from hadrons to QGP occurs as a crossover, while for high valued of μ_B theoretical models predict the existence of a critical point, beyond which a first-order phase transition takes place. Identifying this critical point is one of the main goal in the study of QCD phase transitions. The pseudocritical temperature is used to characterize the approximate temperature at which the QGP transition occurs. lQCD calculations at $\mu_B \sim 0$ estimate it to be around 155 MeV. However, as μ_B increases the temperature decreases and its precise determination is an important topic of research, with experimental efforts focusing on define a more precise QCD phase diagram (Figure 1.2) through varying the energy of beam collisions. It is believed that the QGP state filled the early universe $\sim 10^{-6}$ s after the Big Bang and it froze out into hadrons after $\sim 10 \times 10^{-6}$ s. Hadrons later formed nuclei and so all the known matter.

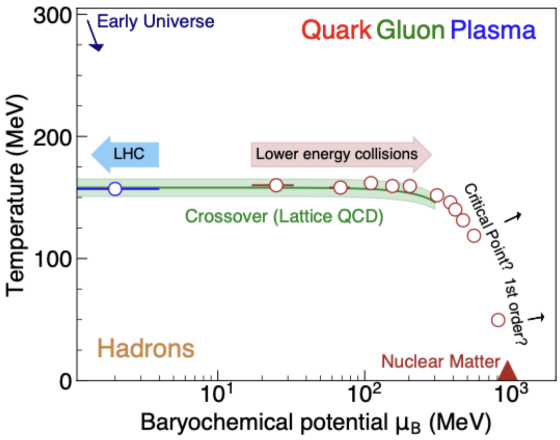

Figure 1.2: QCD phase diagram [4]. The green band shows the μ_B region accessible to lQCD calculations.

In a laboratory, conditions such that of early universe can be created by colliding heavy ions at multi-TeV energy. Such collisions are provided by the LHC at CERN since 2010. In particular, ALICE detector was specifically designed to investigate the QGP created at high energies and the particles produced from collisions.

QGP can be created from the collision of heavy-ions at ultra-relativistic energies. The different stages of a collision are shown in Figure 1.3 and include: (i) an intial state depending on projectiles' wave functions; (ii) large-Q^2 interactions of partons; (iii) low-Q^2 interactions (pre-equilibrium); (iv) equilibrium and expansion of QGP; (v) hadron formation; (vi) freeze-out of hadrons; (vii) detectable stable particles. For an heavy-ion collision it is important to define two crucial geometrical quantities which play an important role in particle production. The first is the impact parameter b, a fundamental geometric quantity that represents the perpendicular distance between the centers of the two colliding nuclei in the plane transverse to the beam direction, quantifying if a collision is central (small b) or peripheral (large b). The second is the pseudorapidity η, which depends on the polar angle θ measured from the beam axis as follow:

$$\eta = -ln\ tan(\theta/2) \tag{1.1}$$

describing the spatial distribution of produced particles.

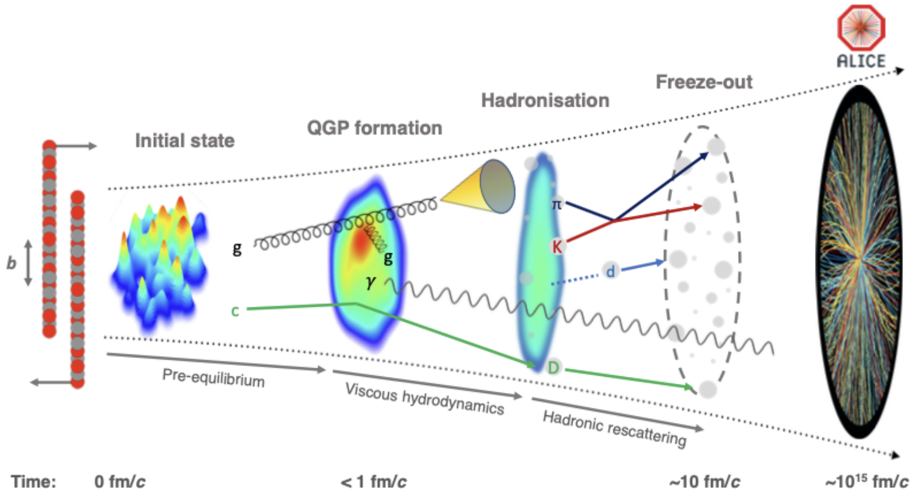

Figure 1.3: Evolution of an heavy-ion collision at LHC energies [4].

When the QGP cools below the transition temperature T_{pc} it will hadronise. The production of particles depends on different aspects, such as the centrality of the collision and the region of their production; indeed, in central collisions more particles are produced with respect to peripheral ones, while the hottest region, where the production is maximal, is the midrapidity region $\eta \sim 0$. In addition, heavy-ion collisions are more effective in transferring the longitudinal beam energy into particle production at midrapidity than pp collisions, and the centrality itself allows to manage the amount of energy deposited in the collision region.

1.2 Physics goals

The unique PID and tracking capabilities of ALICE 3 can provide a complete description of some physics areas. Some examples are presented below.

1.2.1 Heavy flavour probes of QGP

The masses of charm and beauty quarks, $m_c \simeq 1.28$ GeV and $m_b \simeq 4.18$ GeV, are sufficiently larger that the pseudocritical temperature so that thermal production of the two quarks in the QGP is strongly suppressed. On the other hand, at the LHC energies, a large production of heavy-ion quarks is expected to take place via hard scattering processes which can be described using pQCD [5]. As a result, the c and b content of the fireball is determined by initial hard scattering and their annihilation is very small.

ALICE 3 would be able to reduce the statistical uncertainties in the beauty sector thanks to a larger reconstruction accuracy and selection purity of beauty mesons and baryons, like B, Λ_b and Λ_c^+, down to very low p_T (≤ 1 GeV/c). Accurate measurements in the beauty sector are a probe for the theoretical models of quark transport into expanding QGP and allow a microscopic description of heavy-quark interactions.

The mechanism of heavy-quark parton propagation can be studied also through the correlation in the azimuthal angle $\Delta\varphi$ between charm-hadron pairs, like $D\bar{D}$, measured with respect to the p_T, Δp_T and $\Delta\eta$. Measurements of heavy-flavor correlations are still limited in the current ALICE detector due to the pseudorapidity coverage ($|\eta| < 0.9$) and only with ALICE 3 ($|\eta| < 4$) it will be possible to detect back-to-back $D\bar{D}$ with excellent efficiency down to very low p_T. Expected ALICE 3 performances are shown in Figure 1.4.

Limited measurements also affects the charm sector. In Run 3 and 4 precise measurements of baryon-to-meson ratios would be possible only for baryons containing one charm quark, while with ALICE 3 precise measurements of the production yields multi-charm hadrons (Ξ_{cc}^+. Ω_{cc}^+, Ω_{ccc}^{++}, ...) would help our understanding of hadron formation from deconfined QGP.

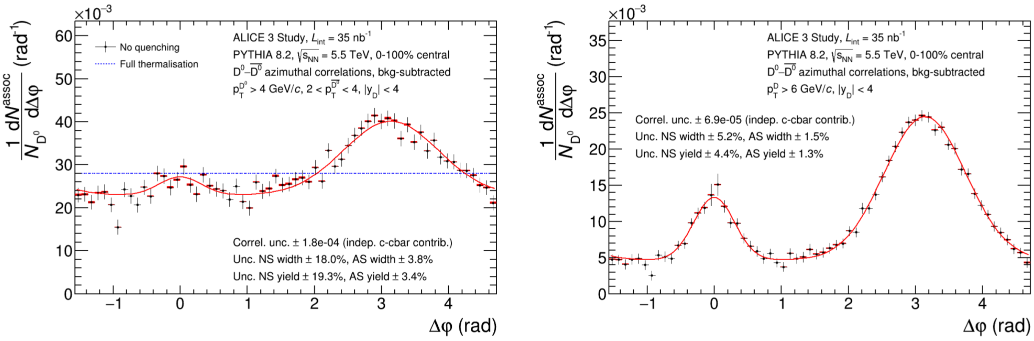

Figure 1.4: Azimuthal distribution of D$\bar{D}$ pairs with $p_{T1} > 4$ GeV/c and $2 < p_{T2} < 4$ GeV/c (left) and $p_{T1} > 6$ GeV/c (right) in Pb-Pb collisions for $|y| = |\eta| < 4$ and $\mathcal{L}_{tot} = 35\ nb^{-1}$ [6].

1.2.2 Quarkonium states

Quarkonium is a heavy flavor q$\bar{\text{q}}$ state that has been considered one of the most impressive signatures for QGP formation. In particular, one of the probes of deconfinement is the charmonium (c$\bar{\text{c}}$); indeed, the J/ψ meson (the grond state of charmonium) is the first hadron for which a meccanism of suppression (melting) was suggested [7]. In the bottomonium sector Υ, a sequential suppression following the radial excitations 1S, 2S and 3S is found, as expected from dissociation in QGP. ALICE 3 will have excellent capabilities in reconstructing the quarkonium states down to $p_T \simeq 0$ and the processes $\chi_c \rightarrow J/\psi\ \gamma$, $\chi_b \rightarrow \Upsilon\gamma$ [1] from pp and heavy-ion collisions will be measured over a wide kinematic range.

1.2.3 Chiral symmetry restoration

Chiral symmetry breaking is evident from the mass spectrum of hadrons and it is closely related to confinement: from lQCD it is shown that the deconfinement phase transition takes place at temperature close to chiral phase transition. Dilepton production at such temperature is sensitive to effects of chiral symmetry restoration via the mesons spectral function. In particular, such restoration would be observed by measuring ρ (770) meson and its chiral partner a_1. The latter is very challenging in heavy-ion collisions. The present ALICE apparatus still produces measurements of thermal dilepton emission with a sizeable background which affects a precise determination of the mass range above the ρ peak. Low-background capabilities and larger statistics will be addressed with low-mass detectors and high vertexing capabilities, in order to access the mass region (0.85-1.2 GeV/c) where $\rho - a_1$ mixing is expected to leave a peculiar signature. Indeed, a low material budget detector helps to reduce multiple scattering and energy loss of particles, which could affect the measurements.

---

[1] χ_c and χ_b are P-wave states (L=1)

1.2.4 Ultra-soft photons

At relativistic energies, a large quantity of photons is produced in hadron-hadron and nuclear collisions, mainly from the decay of mesons, like π^0 and η, and baryons produced in such collisions. Photons are of particular interest to study the hot QCD medium, since they escape it without being affected. The yield of direct photons depends strongly on the considered process and on the hot medium properties. In particular, photons produced in QCD process can be calculated in the pQCD regime since their p_T is sufficiently large, while lQCD methods can be used in the low-p_T region.

In quantum field theories, the production of these very low transverse momenta photons is linked to the charged final state through fundamental theorems, like the Low's theorem [8]. According to the Low's theorem, it is possible to relate hadron momenta produced in a high energy collision to the number of soft photons produced. Low's theorem can be used to quantitatively test the infrared limits of QED and QCD. Thanks to its ultra-low mass tracker, ALICE 3 plans to perform measurements in the sub-leading p_T range to study the approach to the Low limit. A specifically designed, small spectrometer at forward rapidity in the range $3.5 < |\eta| < 5$, will reach the measurements in the range of $1\ \mathrm{MeV}/c < p_T < 100\ \mathrm{MeV}/c$.

1.3 Detector concept

In Section 1.2 was shown that for large part of key measurements of the future programmes the resolution current ALICE detector is limited. Only with ALICE 3 it would be possible to rely on superb tracking and PID capabilities to access very low-p_T regions. Some of the kinematic range of interest for ALICE 3 presented in Section 1.2 are summarized in Table 1.1

Observables	**Kinematic range**
Heavy-flavour hadrons	$p_T \to 0, \|\eta\| < 4$
Dielectrons	$p_T \approx 0.05$ to 3 GeV/c^2, $M_{ee} \approx 0.05$ to 4 GeV/c^2
Photons	$p_T \approx 0.1$ to 50 GeV/c, $-2 < \eta < 4$
Ultra-soft photons	$p_T \approx 1$ to 50 MeV/c, $3 < \eta < 5$
Quarkonia and exotica	$p_T \to 0, \|\eta\| < 1.75$
Nuclei	$p_T \to 0, \|\eta\| < 4$

Table 1.1: A summary of the main physics goals along with their kinematic range of interest of ALICE 3 [6].

ALICE 3 is a nearly massless and very compact (radial dimension ~ 1.2 m, longitudinal dimension ~ 4 m) detector which consists of a central barrel to cover the pseudorapidity region $|\eta| < 1.4$ and two endcaps to extend the region up to $1.4 < |\eta| < 4$. The central barrel is composed of a 3-layers Inner Tracker (IT) located inside the beam pipe, an Outer Tracker (OT) and a Time-of-Flight (TOF) detector. The whole apparatus is programmed to be embedded in a solenoidal superconducting magnet of 2 T, needed to keep high tracking efficiency at few tens of MeV/c transverse momenta while maintaining good resolution ($\sim 2\%$) at high momenta (~ 30 GeV/c). A schematic of ALICE 3 apparatus is shown in Figure 1.5, followed by the illustration of the main subdetectors with their basic properties

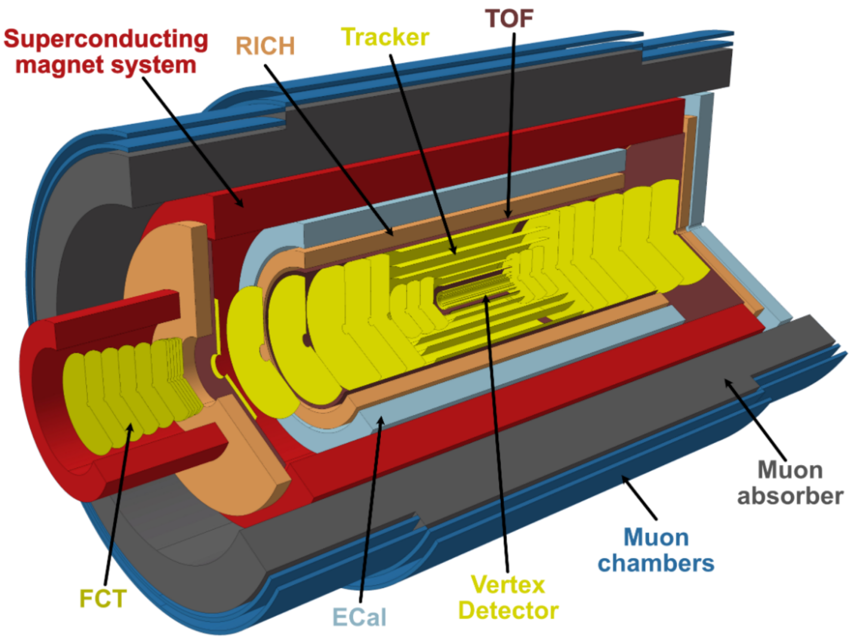

Figure 1.5: ALICE 3 detector concept [6].

Tracking system

A silicon pixel tracker is the core of the particle reconstruction system of ALICE 3. The outer tracker consist of 8 cylindrical layers and 9 forward discs on either side of the interaction point and each layer is responsible for $\sim 1\%$ of the radiation length in the material. The momentum resolutions, due to a 2T magnetic field and forward dopiles, varies form $\sim 0.6\%$ at midrapidity to $\sim 2\%$ at $|\eta| = 3$ and $\sim 1\%$ up to $|\eta| = 4$.
The vertex detector, with an inner radius of 5 mm, consists of 3 cyclindrical layers and 3 disks on either side. Its superb position resolution approach ~ 2.5 mm with $\sim 1‰$ of radiation length for the first layer.

Particle identification system

The particle identification layers includes the timing system, carried out with two TOF detector layers with 20 cm (inner) and 85 cm (outer) radius and a time resolution of $\simeq$ 20 ps. It allows to identify electrons and hadrons up to $p_T \simeq 500$ MeV/c and 2 GeV/c (π/K separation). An inner TOF layer is foreseen at 20 cm radius for particles below 300 MeV/c.

Behind the TOF, a Ring Imaging Cherenkov detector (RICH) (refractive index $n = 1.03$) is foreseen, providing an excellent separation of electrons and pions up to 2 GeV/c and protons from e, π and K up to 14 GeV/c.

A muon chamber and a muon absorber are planned to be installed outside of the magnet and they will detect and match the muon tracks to tracks in the silicon pixel tracker. The absorber would be very efficient for muons down to $p_T \sim 1.5$ GeV/c, needed to reconstruct the J/ψ at rest at $\eta = 0$.

Another variety of measurements, like jets and χ_c decay, will be possible due to an electromagnetic calorimeter (ECal) covering the barrel acceptance and one forward direction. $PbWO_4$ crystals around midrapidity region would provide the detection of direct photons in the thermal emission regime and the separation of $\chi_c \rightarrow J/\psi\ \gamma$ decays. However, ultra-soft photons down to 1 MeV/c are quite challenging and requires the application of the Lorentz boost at larger η ($\eta \sim 4$). In particular, $e^{\pm}$ pairs from photon conversion are thought to be reconstructed with a Forward Conversion Tracker (FCT) installed at forward $3 < \eta < 5$ and made of an array of silicon pixel disks.

1.3.1 Sensors technology

Vertexing, tracking and timing detectors of ALICE 3 will rely on ultra-thin silicon detectors technology which are being studied in an intensive R&D programme. Tracker layers are based on CMOS (Complementary Metal–Oxide Semiconductor) MAPS (Monolithic Active Pixel Sensors) transistor technology, still present on ITS2, whose optimisation would make them withstand $\sim 1 \times 10^{15}$ 1 MeV $\mathrm{n}_{eq}/\mathrm{cm}^2$ almost without being degraded at -30^o C [9]. The vertex detector needs wafer-sized sensors with excellent position resolution of $\sim 2.5\mu$m while for the outer tracker a reticle-size sensor of a few cm^2 will be used, with a spatial resolution $\sim 10\mu$m.

For the timing layers, three main sensors technologies are being considered: fully depleted CMOS MAPS sensors, a CMOS LGAD (Low-Gain Avalanche Diodes) and Single Photon Avalanche Diodes (SPAD). At present, the smallest time resolution with CMOS is possible only for fully-depleted sensors, thus only with fast charge collection, it has not approached yet a time resolution of 20 ps. Standard LGADs, instead, rely on a thin gain layer in order to increase the signal-to-noise ration. LGADs demonstrate very good timing resolution of 30-20 ps and radiation hardness and have been widely developed and used in HEP physics, like ATLAS and CMS experiments [10, 11]. Recent measurements of the ALICE3 INFN-Bologna group [12] demonstrate the possibility to improve the time resolution of Ultra Fast Silicon Detectors (UFSDs) based on the LGAD technology by reducing the sensor thickness from the standard 50 μm, as shown in Figure 1.6.

SPADs in array configuration in SiPMs (Silicon PhotoMultipliers) are being considered as well for the TOF layers and this work is presented in this context. A more detailed description of SiPM will be provided in Chapter 3.

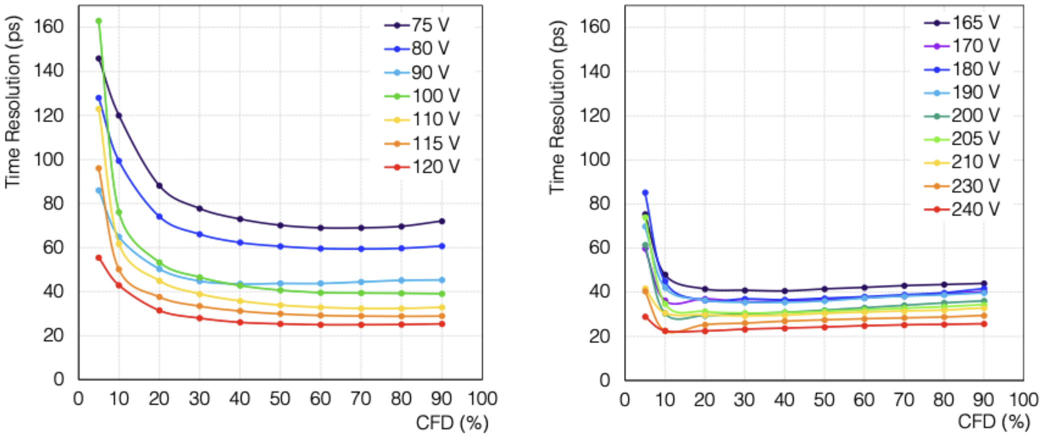

(a) (b)

Figure 1.6: Measured time resolution versus the Constant Fraction Discrimination (CFD) threshold for several applied voltages for (a) 25 μm and (b) 25 μm thick LGADs [12].

1.3.2 TOF

One of core of the particle identification (PID) is a TOF detector with a goal time resolution of 20 ps, able to provide a PID over the full acceptance ($|\eta| < 4$) and to identify hadrons and electrons up to $p_T \sim 500$ MeV/c. TOF detector is expected to be installed at ~ 1 m from the beam line, surrounding the central tracker, and it will be divided in three parts. Two layers of barrel TOF (iTOF (inner) and oTOF (outer)) are respectively located at 20 cm and 105 cm from the beam pipe. The most stringent TOF layers requirements comprehend a power resolution < 50 mW/cm^2 and a time resolution of $\simeq$20 ps. The combination of iTOF and oTOF is not only important for reliable time-of-flight measurements but also for the precise determination of the start time [2]. Other specifications are reported in Table 1.2.

---

[2] The start time is already determined by TOF with a resolution of ~ 3 s in high-multiplicity events

	iTOF	**oTOF**	**fTOF**
Radius (m)	0.19	0.85	0.15-1.5
z range (m)	-0.62-0.62	-2.79-2.79	4.05
Surface (m^2)	1.5	30	14
Granularity (mm^2)	1×1	5×5	1×1 to 5×5
Hit rate ($\mathrm{kHz/cm}^2$)	74	4	122
NIEL (1 Mev $\mathrm{n_{eq}/cm^2}$)/month	1.3×10^{11}	6.2×10^{9}	2.1×10^{11}
TID (rad)/month	4×10^{3}	2×10^{2}	6.6×10^{3}
Material budget ($\%X_0$)	1-3	1-3	1-3
Power density ($\mathrm{mW/cm}^2$)	50	50	50
Time resolution (ps)	20	20	20

Table 1.2: ALICE 3 specifications of the inner TOF (iTOF), the outer TOF (oTOF) and the forward TOF (fTOF) [6].

The PID of light nuclei will be mostly based on the TOF measurements and able to distinguish the nuclei with different m/z. In this context charge-sensitive measurements are crucial in order to solve the ambiguity for nuclei sharing the same m/z. Figure 1.7 shows the response of the TOF system for simulated Pb-Pb collisions in a magnetic field of B = 2T. As it can be seen, due to the larger occupancy, the fake hit association is larger for the iTOF and it is responsible for the increasing background due to track-TOF mismatch.

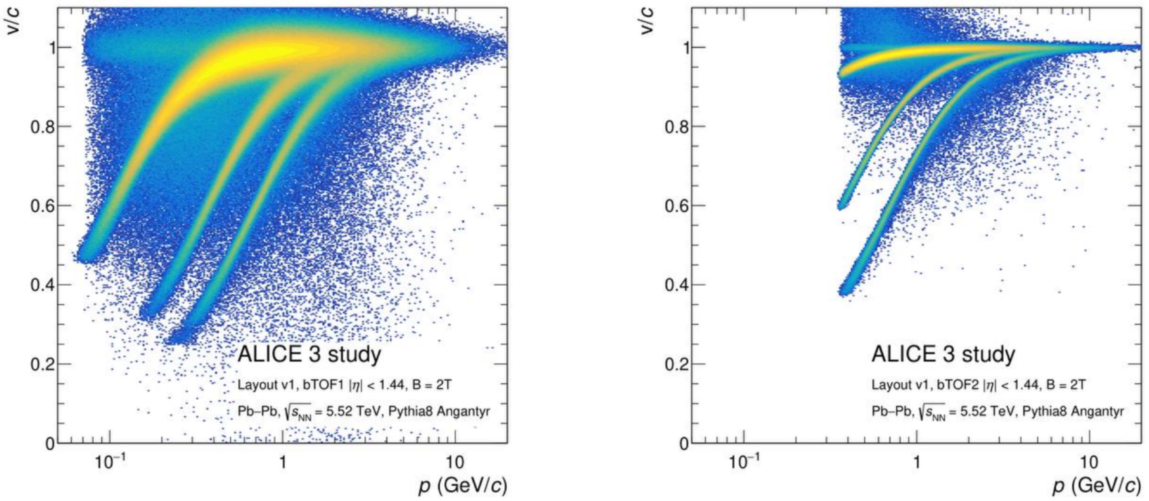

Figure 1.7: Particle velocity as a function of the momentum simulated with the iTOF (left) and oTOF (right) in Pb-Pb collisions in a B = 2T magnetic field [6].

TOF and RICH

Time-of-flight is not the only technique for particle identification in the central barrel detector and in the forward region. Indeed, also Cherenkov imaging technique is used. The barrel RICH (bRICH) is made of a 2 cm thick aerogel detector with refractive index $n = 1.03$ located behind the TOF at 110 cm from the beam line, with an average angular resolution of 1.5 mrad. RICH detector would extend the e/π separation up to 2 GeV/c, the π/K separation up to 10 GeV/c and the K/p up to 14 GeV/c. Figure 1.8 summarizes the PID capabilities for simulated 3σ separation in Pb-Pb events, defining the $\eta - p_T$ region where PID is possible with a separation of at least 3σ.

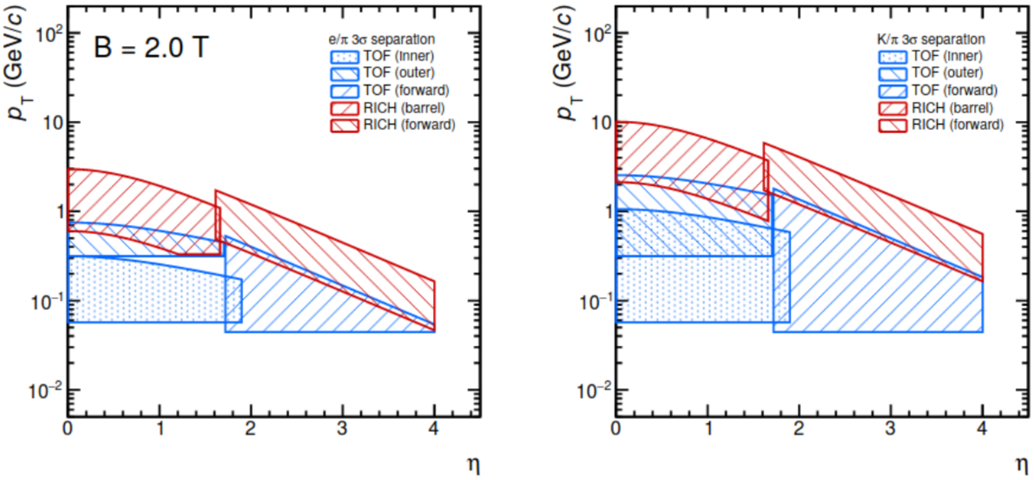

Figure 1.8: Analytical calculations of the $\eta - p_T$ regions in which particles can be separated by at least 3σ in a 2 T magnetic field [6].

Recent studies [13, 14] have explored the possibility to combine the TOF and the RICH into a single detector to enlarge the sensitivity and the precision of the two detectors. The system consists of a Cherenkov radiator layer separated from a photosensitive surface equipped with SiPMs by an expansion gap. A thin glass slab, acting as a second Cherenkov radiator, is coupled to the SiPMs to perform Cherenkov-based TOF measurements. SiPMs seem to be good candidates for the two subdetectors, as they can detect both minimum ionizing-particles and single photons with high efficiency and good timing.

Chapter 2

Solid-state detectors

Solid-state detectors are based on semiconductor materials like germanium and silicon and they are widely used both inside and outside the High-Energy Physics (HEP) field. The wide availability of silicon and their peculiar features, such as the possibility of working at room temperature, makes them the first choice withing detectors for HEP experiments. In this chapter are reported the main concepts of the physics of semiconductor detectors and their features, especially useful for time measurements applications. In particular, the focus is on the SiPM device, a silicon detector traditionally coupled to scintillators and optimized for light detection but here considered also for its possibility to directly detect charged particles. Indeed, the main results of this thesis work, shown in the last chapter, rely on this latter possibility.

2.1 Physics of semiconductor detectors

In a semiconductor material the gap between the conduction band and the valence band is quite small $\sim$ 1 - 3 eV. The two primary semiconductors elements, Germanium and Silicon, belong to the IV group, therefore they have four valence electrons and form four covalent bonds. As the temperature increase from 0 K to room temperature (consider T=300 K) one of these electrons can be thermally excited to the conduction band, breaking the covalent bond and leaving a vacancy (or hole) which is positively charged and can be filled, which can be filled in turn by a neighboring valence electron.

The process can be repeated, creating an hole current. Therefore, by applying an electric field in a semiconductor the total current has two contributions: the electrons and the hole current. At room temperature the concentration n of electrons in the conduction band and the concentration p of holes in the valence band is the same and is called intrinsic concentration of charged carriers n_i in silicon:

$$n_i = n = p = 1.45 \times 10^{10} \text{cm}^{-3} \tag{2.1}$$

The intrinsic concentration concentration can be computed from the Fermi-Dirac statistics and the density of states as:

$$n_i = \sqrt{N_C N_V} e^{\frac{-E_g(0)}{2kT}} \tag{2.2}$$

where $E_{g(0)}$ is the band gap energy at T=0 K, k is the Boltzmann constant and N_C, N_V are the effective densities of states in the conduction and valence band respectively, depending on the effective masses of the electrons and holes respectively.

For fields up to 10^4 V/cm the drift velocity which transports the charged carriers is proportional to the applied electrical field E. For electrons and holes, the drift current densities are, respectively:

$$J_{n,drift} = (-q)nv_D = qn\mu_n E \tag{2.3}$$

$$J_{p,drift} = (+q)pv_D = qp\mu_n E \tag{2.4}$$

where $\mu_n \sim 1350$ cm^{2}Vs^{-1} and $\mu_p \sim 450$ cm^{2}Vs^{-1} are the electron and hole mobilities in silicon at room temperature, and $v_D = \mu E$ is the drift velocity. This relation between velocity and the field saturates above 10^4 V/cm, where v_D becomes constant ($\sim 10^7$ cm/s). However, the total process must take into account also the diffusion current, whose density is proportional to the gradient of the carrier density:

$$J_{n,diff} = qD_n \nabla n \tag{2.5}$$

$$J_{p,diff} = -qD_p \nabla p \tag{2.6}$$

where D_n and D_p are the diffusion coefficients, with typical values of 35 cm^{2}s^{-1} and 12.4 cm^{2}s^{-1} at room temperature respectively. The equations above shows that the negative charges of the electrons diffuse a current pointing in the direction of the gradient, and viceversa according to holes. The total current density combine both contributions from drift and diffusion processes:

$$J_n = J_{n,drift} + J_{n,diff} = q(n\mu_n E + D_n \nabla n) \tag{2.7}$$

$$J_p = J_{p,drift} + J_{p,diff} = q(p\mu_p E - D_p \nabla p) \tag{2.8}$$

In case of silicon, the semiconductor exhibits an indirect bandgap structure. Since phonons are required to satisfy momentum conservation when an electron transitions from the valence band to the conduction band, the energy required to generate an electron-hole pair exceeds the bandgap energy and is approximately 3.62 eV. The, if we consider a mean ionization energy $I_0 = 3.62$ eV, a silicon thickness $d = 300$ μm and a MIP $dE/dx = 4$ MeV/cm, we obtain that the MIP signal in the detector is:

$$\frac{dE/dx \ \cdot \ d}{I_0} \simeq 10^4 \ \mathrm{e^-h^+} \text{ pairs} \tag{2.9}$$

While, if we look at charge carriers thermally created in intrinsic silicon with same thickness and area $A = 1$ cm^2 at 300 K we have:

$$n_i dA \simeq 10^8 \text{ e}^-\text{h}^+ \text{ pairs} \tag{2.10}$$

These thermal pairs dominates the pairs from impinging particles and the charged signal is then lost. For this reason, intrinsic silicon crystals are not used but a depleted zone, free from charge carriers, is developed through the doping of silicon.

Furthermore, the charge-carrier concentration is very small and even if the number of holes is equal to the number of electrons, their mobility is very different. These problems are usually solved by doping the pure semiconductor crystals with impurity atoms belonging to the third (trivalent) or the fifth (pentavalent) group, which substitute the semiconductors atoms in the lattice. Thanks to the impurities, the energy level is very close to that of valence or conduction band. At room temperature of T = 300 K the thermal energy is of the same order of the energy needed to ionize the dopant, called activation energy, and all acceptors (trivalent) and donors (pentavalent) are ionized. The effect of doping with acceptors is to create an excess of holes and to decrease the number of electrons. On the contrary, doping with donors creates an excess od electrons and decreases the number of holes. In n-doped semiconductor at room temperature $n \gg p$, so $n \sim N_D$ where N_D is the donor concentration while in a p-doped element $p \gg n$, so $p \sim N_A$ where N_A is the acceptor concentration.

When a p-doped region is put in contact with a n-doped region the so called P-N junction is formed (Fig. 2.1). Here, the electrons diffuse from n-doped region to the p-doped while holes follows the opposite until equilibrium is reached: an electric field is generated and stops the diffusion process.

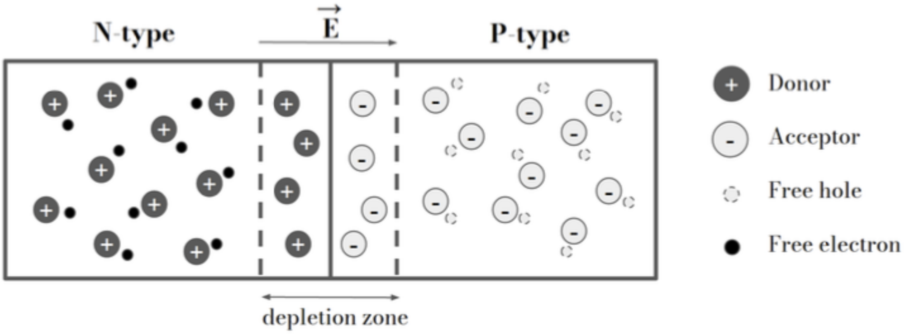

Figure 2.1: Scheme of a P-N junction [15].

In such configuration, an intermediate space of region without charge carriers called depletion region is created at the junction. Therefore a built-in voltage difference V_{bi}, also called contact potential, is established across the junction from the n-side to the p-side. This potential is expressed as:

$$V_{bi} = V_T ln \left(\frac{N_A N_D}{n_i^2} \right) \tag{2.11}$$

where $V_T = T/11600$ V is the equivalents of the temperature expressed in Volt and $N_{A,D}$ are the acceptors and donors concentrations. Typically V_{bi} is below 1 V. P-N junctions are usually asymmetrically doped with, for example, $N_A > N_D$ so that the depletion region penetrates more in the lighter-doped region and if the material is heavily doped, the width of the depletion region can be neglected.

At thermal equilibrium the electric force and diffusion force compensate, but the application of an external voltage can increase or decrease the width of the depletion region. The junction is polarized in forward, or direct, bias when the voltage is applied with the anode on the p-side and the cathode on the n-side while is polarized in reverse bias when the voltage is applied with the anode on the n-side and the cathode on the p-side. In the first case a net diffusion current of electrons and holes flows across the junction and the depletion region will become narrower, while in the second electrons and holes moves away from the depletion region, which will become larger. The described configurations are shown in Fig. 2.2.

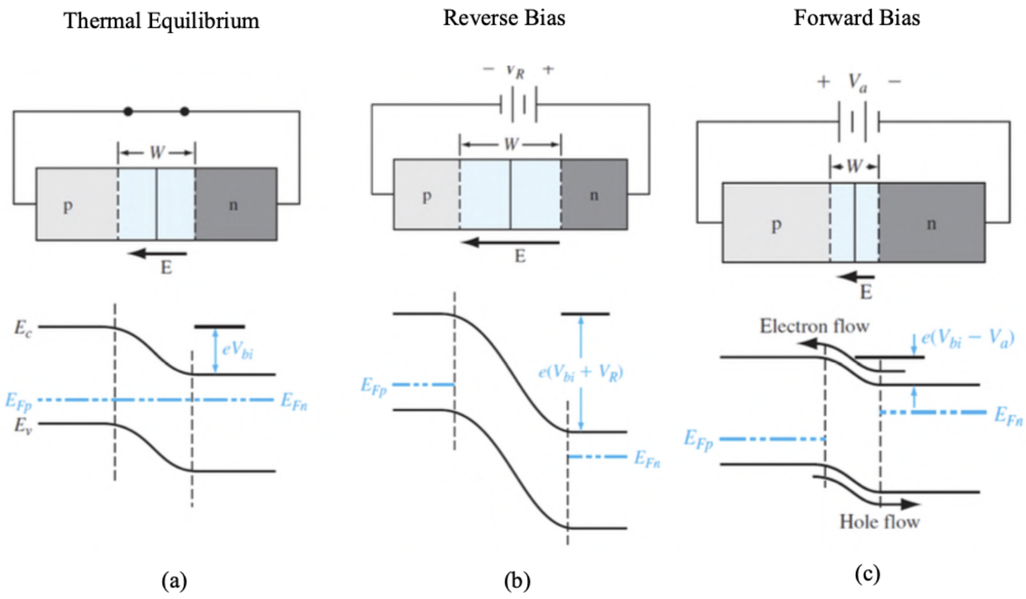

Figure 2.2: Scheme of a P-N junction in case of no bias applied (a), reverse bias (b) and forward bias (c).

The ideal current-voltage (I-V) characteristic of a P-N junction is given by:

$$I = I_0 \left(e^{\frac{eV_{app}}{kT}} - 1 \right) \tag{2.12}$$

where V_{app} is the applied voltage, which can be positive or negative and J_s is the saturation reverse current density, defined by:

$$I_0 = \frac{eAD_p p_n(0)}{L_p} + \frac{eAD_n n_p(0)}{L_p} \tag{2.13}$$

where $L_{n,p}$, $D_{n,p}$ are the diffusion length and coefficient for electrons and holes respectively and $p_n(0)$, $n_p(0)$ are the initial hole/electrons concentration in the n/p side. In a semiconductor diode, a real example of a P-N junction, the I-V characteristic suddenly drops beyond a certain value of reverse voltage, entering in the breakdown region. The breakdown mechanism can occur due to tunneling effect, when the conduction and the valence bands are sufficiently close that electrons can directly pass from the valence band in the p-side to the conduction band in the n-side (Zener breakdown), or due to electrons and holes that, moving in the depletion region, acquire enough energy from the electric field to create secondary pair in the depletion region. However, also in the forward bias the I-V characteristic deviates from the ideal behavior, by increasing voltage, due to internal resistive effects. The I-V curve for a diode is shown in Figure 2.3.

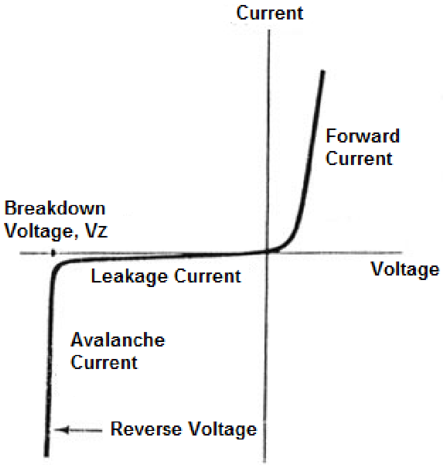

Figure 2.3: A P-N junction characteristic.

2.2 Particles interaction with silicon

In a silicon detector, the depletion region creates an area where no free charge carriers exist, making it sensitive to incoming radiation. When charged particles or photons interact with the detector, they transfer energy to electrons in the silicon, exciting them from the valence band to the conduction band, creating electron-hole pairs. These electron-hole pairs are the only mobile charges in the depletion region and are influenced by the applied electric field. Under an electric field $E > 10^4$ V/cm electrons travel 1 μm of silicon in 15 ps and they move towards the anode, while the holes, taking 30 ps, move towards cathode (Figure 2.4). As the electrons and holes move they induce signal which is measurable. The signal begins when the carriers start moving and ends when all of them have reached their respective collection electrodes. The time it takes for the charge carriers to travel through the silicon depends on their mobility. In a typical silicon detector with a thickness of 300 μm, the electrons take $\sim$ 10 ns to reach the anode, while the holes take $\sim$ 25 ns to reach the cathode.

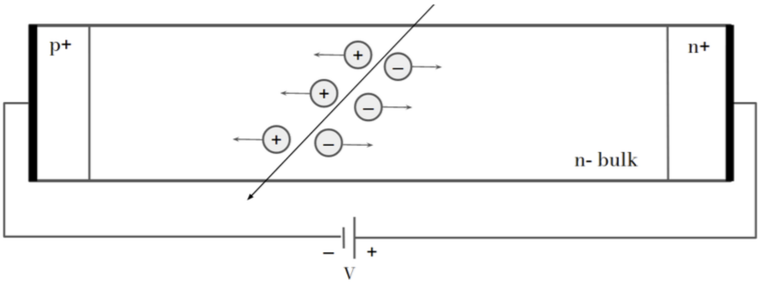

Figure 2.4: P-N junction principle of operation [15].

2.2.1 Photons

When a photon passes through matter, it can interact in several ways, depending on the photon's energy and the material properties. The key interaction mechanisms are photoelectric effect, Compton scattering, and pair production, each of which dominates in different energy ranges.
At lower photon energies, the photoelectric effect is the dominant interaction mechanism. In this process, a photon is absorbed by an atom, causing the ejection of an inner-shell electron. The photon's energy is transferred to the (photo)electron and the vacancy in the electron shell is filled by an electron from a higher energy level.
As the photon energy increases (around 1 MeV), Compton scattering becomes more significant. In this process, a photon interacts with a weakly bound electron, transferring part of its energy to the electron and causing it to be expelled. The photon loses energy and changes direction, but it is not completely absorbed.
Above 1 MeV pair-production is dominant: the photon is completely absorbed near the nucleus of the atom, and its energy is used to produce an electron-positron pair.
The intensity I of a photon beam passing through matter decreases as the photons interact with the material, according to the following attenuation law:

$$I(x) = I_0 e^{-\alpha x} = I_0 e^{-x/d} \tag{2.14}$$

where I_0 is the initial intensity, α is is the absorption coefficient which is equal to the inverse of the mean free path of a photon i.e. the penetration depth d.

The average d for standard silicon at 300 K in the range ∼ 200-1110 nm as a function of incident light wavelength is shown in Figure 2.5a. Here, d is ∼ 0.1 μm at 400 nm at N-UV wavelengths, ∼ 2.5 μm at 600 nm visible light wavelength and ∼ 10 μm at ∼ 780 μm IR wavelengths. A wavelength in the N-UV of 300-400 nm which corresponds to energies of 4-3 eV is absorbed in silicon in the first 0.1 μm as can be seen in Figure 2.5b where α and d are shown as a function of the photon energy in eV.

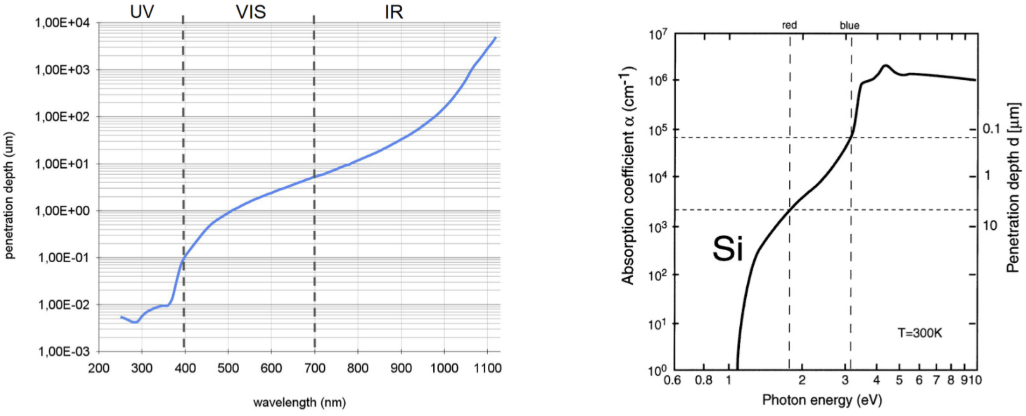

(a) (b)

Figure 2.5: (a) Penetration depth d of intrinsic silicon at 300 K as a function of the incident wavelength [16]. (b) Absorption coefficient α and penetration depth d of light in silicon at 300 K [17].

2.3 Silicon detectors for timing applications

As mentioned in the previous section, the drift velocity of charge carriers saturates for high electric field applied, so that electron and holes what distance in what time. Such features contribute to make silicon detectors ideal in timing applications, both inside and outside the HEP field.

2.3.1 Time resolution

The main components of a complete timing system (Fig. 2.6) are the detector, i.e. the sensor, which can be described as a capacitance C_d in parallel to a current generator I_{in}, the signal amplifier, the discriminator, that compares the analog signal to a digital threshold converting it in a logical signal, and a Time-to-Digital Converter (TDC) that measures the time interval between the detector signal and the particle trigger, which can be an external detector.

Considering this measurement chain, the total time resolution can be expressed as:

$$\sigma_{tot}^2 = \sigma_{jitter}^2 + \sigma_{current}^2 + \sigma_{slewing}^2 + \sigma_{TDC}^2 \tag{2.15}$$

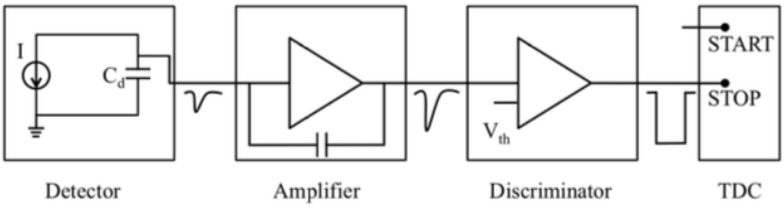

Figure 2.6: Scheme of a time measurement chain [18].

The jitter contribution σ_{jitter} is due to the presence of noise and can be written as:

$$\sigma_{jitter} = \frac{\sigma_N}{\left|\frac{dV}{dt}\right|_{V_{th}}} = \frac{t_r}{\frac{S}{N}} \tag{2.16}$$

where t_r is the rising time, σ_N is the RMS of the noise and $|dV/dt|_{V_{th}}$ is the slope calculated at the threshold value. Therefore, when the signal is rising, the threshold comparator can trigger early or late depending on the noise.

The current contribution $\sigma_{current}$ reflects the stochastic nature of the energy deposition by the MIP in the silicon which follows a Landau distribution in thin detectors. Small variations in the energy release have as a consequence variations of the current. $\sigma_{current}$ is related to the Shokcley-Ramo theorem [19] according to which the initial current in a silicon detector does not depend on the thickness of the sensor but only on the saturated velocity and the number of pairs created per μm:

$$i \propto Nqv \tag{2.17}$$

The time sleewing, or time walk, term is linked to the analog-to-digital conversion of the signals and their comparison with a fixed threshold. Therefore it is associated to the amplitude of the signal, i.e. the deposited charge. This effects can be corrected by analyzing the maximum amplitude of the signal The instant t_d in which a signal with amplitude S overcome a threshold V_{th} is proportional to:

$$t_d \propto \frac{t_r V_{th}}{S} = \frac{V_{th}}{dV/dT} \tag{2.18}$$

Saying N the noise amplitude, the time resolution due to the time sleewing effect is:

$$\sigma_{sleewing} = [t_d]_{RMS} \propto \left[\frac{N}{dV/dt}\right]_{RMS} \tag{2.19}$$

The TDC contribution is related to the process of digitization of the time performed by the TDC. The delay between the start and the end of the signal is given by the number n of clocks cycles each one with a duration Δt . The contribution from the TDC can be expressed as:

$$\sigma_{TDC} = \frac{\Delta t}{\sqrt{12}} \tag{2.20}$$

2.3.2 Gain

The time resolution of silicon detectors suffers the presence of noise (see Section 2.4.2) and for this reason an internal avalanche process is often exploited in silicon timing applications as a source of gain to increase the amplitude of the signal. Figure 2.7 shows the different operation modes for solid state detectors. SPADs (Single Photon Avalanche Diodes) are APD (Avalanche Photo-Diodes) working in Geiger mode, i.e. at high V_{bd} values above which the avalanche starts in a self-sustained process with gain $> 10^4$.

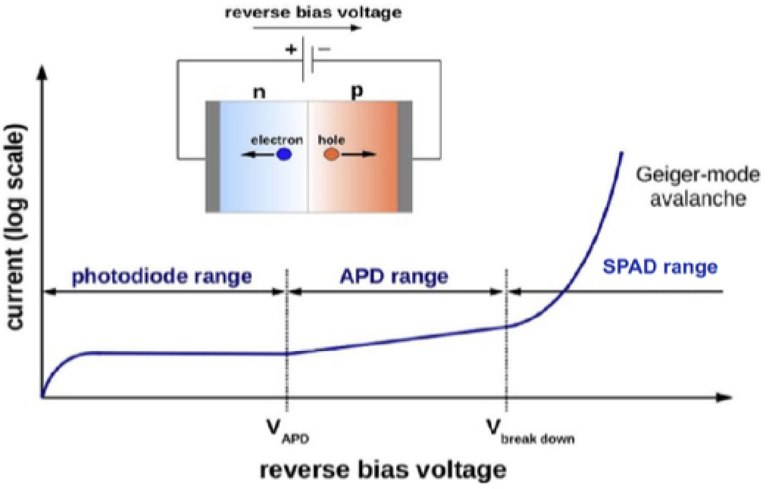

Figure 2.7: Different operation modes for solid state silicon detectors showing: Photodiode (linear, no gain), Avalanche PhotoDiode APD (linear, gain of 50-500) and Geiger mode APD or SPADs (gain $> 10^4$) [20].

2.4 Silicon PhotoMultiplier (SiPM)

The Silicon PhotoMultipier is a sensor (Fig. 2.8) in which both electrons and holes contribute to the avalanche. It is an array of SPADs with order of 10^3 pixels in a total area of few mm^2, where the size of a pixel is 20-100 μm. They operate in Geiger mode with a gain up to 10^6. Each SPAD produce a "binary" signal if it is hit or not, making the SiPM capable of single photon detection.

The SiPM structure is made up different doped layers: the p^+ substrate, the depletion region were photon conversion takes place, the junction made by a p^+ layer (1-3 μm thick) and a n^{++} layer (0.1-1.5 μm). Each pixel has its own quenching resistor needed to stop the Geiger discharge. A structure scheme is reported in Fig. 2.9.

In particular, a SPAD can be modeled as a resistor R_d of ~ 1 kΩ and a capacitance (representing the depletion region) C_d of ~ 10 fF in parallel. In order to stop the

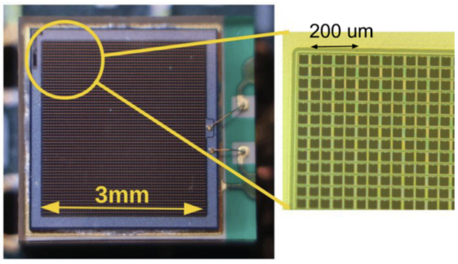

Figure 2.8: Picture of a $3 \times 3\text{mm}^2$ area SiPM with enlargement on pixels.

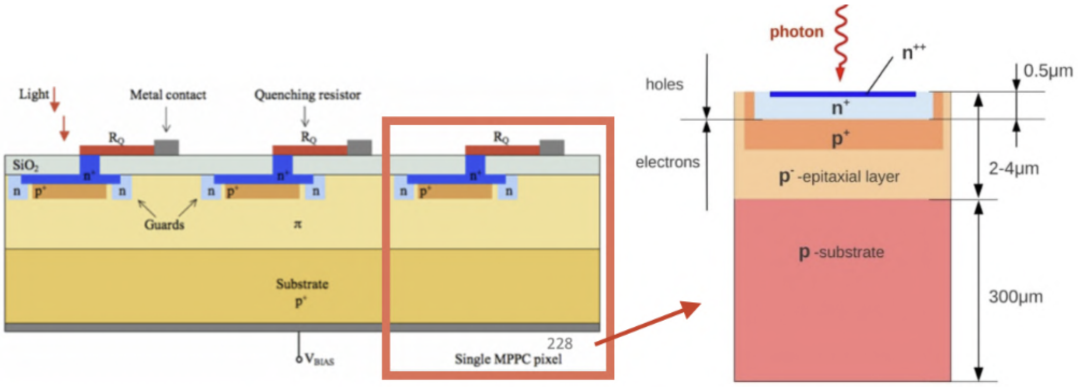

Figure 2.9: Scheme of a SiPM structure with a zoom on the structure of single SPAD. π layer is the depletion region.

avalanche, a series of quenching resistors R_q of 10 kΩ − 10 MΩ is in parallel to capacitance C_q of the order of fF (Figure 2.10). The passage of a particle closes the switch of the equivalent circuit, generating a n-exponential drop in the node $C_d - C_q$ whose discharge follows the discharge time constant τ_d

$$\tau_d = R_d(C_q + C_d) \tag{2.21}$$

where the resistance R_q can be neglected due to its high value. Meanwhile C_q charges through R_d, until the current through R_d reached a threshold value I_d:

$$I_d \simeq \frac{V_{OV}}{R_q + R_d} \sim \frac{V_{OV}}{R_q} \tag{2.22}$$

where the overvoltage OV is defined as $V_{OV} = V_{bias} - V_{bd}$, i.e. the difference between the applied voltage and the breakdown voltage. Therefore, the avalanche is "quenched" and the cells recoveries with a recharge time constant of:

$$\tau_r = R_q(C_q + C_d) \tag{2.23}$$

In a SiPM, the outputs of all the pixels are usually joined together via the quench resistor to a single output node, so that the output signal is proportional to the number of activated cells. The gain of the SPAD can be deduced by:

$$G = \frac{(V_{bias} - V_{bd})C_d}{q} \tag{2.24}$$

which typical value sets in the order of 10^6, giving an excellent capability of photodetection. In particular, the total SiPM capacitance C can be approximated as:

$$C = C_{pixel} \cdot N_{pixel} \tag{2.25}$$

where N_{pixel} is the number of pixel and a single pixel is approximated to be a parallel plan capacitor with capacitance C_{pixel} and high voltage is considered so that parasitic and quenching capacitance of the pixels are negligible.

The breakdown voltage V_{bd} increases with the thickness of the depletion region and, as it increases it becomes more temperature dependent. For that reason it is convenient working with thin depletion region, sensitive from blue to UV light.

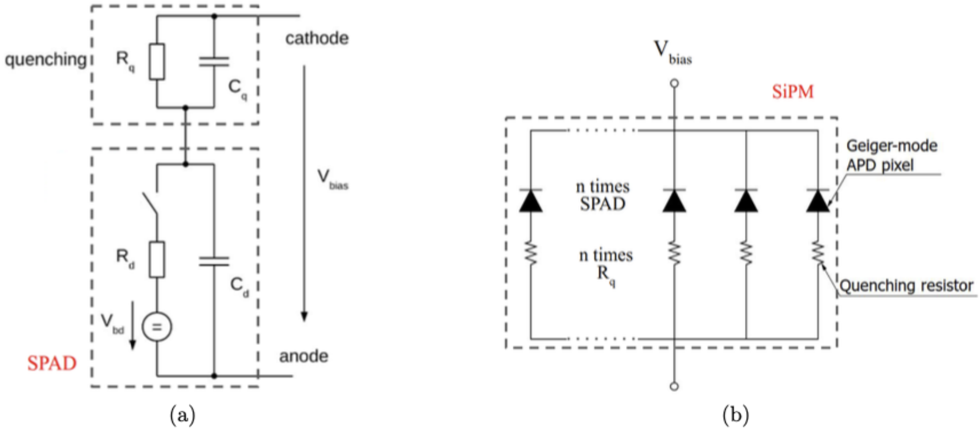

Figure 2.10: Equivalent circuit of a SPAD (a) and of a SiPM (b).

If the incident photon flux is low enough, each cell is hit with high probability by a single photon, so that the total number of hit cells is proportional to the light intensity, i.e. to the number of incident photons. Therefore the total analog output signal is proportional to the number of photons (linear response region) but for high light intensity it deviates from linearity (saturation) since more photons can hit the same cell. The number of fired cells can be expressed as a function of the number of photons and the total number of SPADs, under the assumption of uniform illumination [21]:

$$N_{fired} = N_{tot}\left(1 - exp\left(\frac{-N_{photon} \cdot PDE \cdot ENF}{N_{tot}}\right)\right) \tag{2.26}$$

where PDE and ENF are the Photon Detection Efficiency and the Excess Nois eFactory respectively, explained more in details in the following subsections.

2.4.1 PDE

The Photon Detection Efficiency (PDE) is the quantity describing the sensitivity for the sensor down to single photon detection. It is defined as the ration between the number of detected photons and the number of incoming ones, and it is given by:

$$PDE = Q_E \cdot P_T \cdot FF \tag{2.27}$$

where Q_E (70-80%) is the quantum efficiency, i.e. the number of pairs created per incident photon, P_T ($\sim$ 90%; lower than 100% due to doping inhomogeneities) is the Geiger (breakdown) probability and FF (30-80%, depending on SiPM technology and design) is the geometrical fill-factor, defined as the fraction of the sensitive area over the total cell area of the SiPM:

$$FF = \frac{\text{active area}}{\text{total area}} \tag{2.28}$$

.

Typical maximum value of the PDE are between 40% and 60%, depending on the photon wavelength λ, as shown in Figure 2.11 (a). For example, a red photon ($\lambda \sim$ 700 nm) has an absorption depth of few μm so it is absorbed in the intrinsic layer (π) while a blue photon ($\lambda \sim$ 450 nm) has an absorption depth of $\sim$ 0.5 μm so it is absorbed in the n$^+$ layer, close to the junction. In Figure 2.11 is shown the PDE at different OV of sensor prototypes NUV-HD by FBK, proving a peak of 40%-55%, making these sensors well suited for Cherenkov light detection [22].

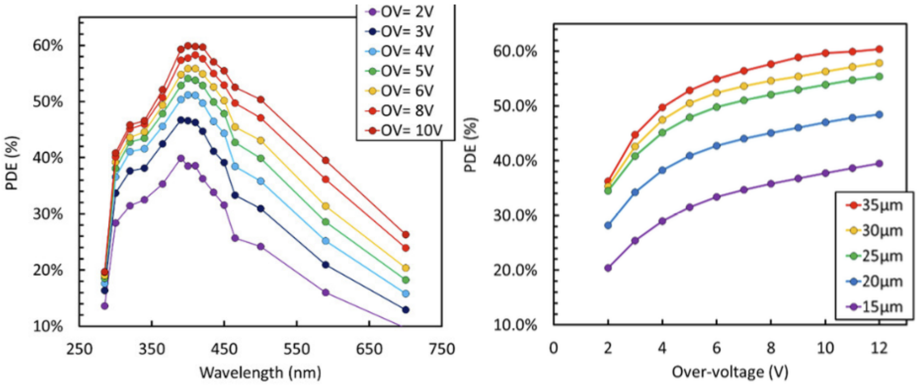

(a) (b)

Figure 2.11: PDE as a function of the wavelength at different overvoltages (a) and as a function of overvoltage at different cell pitches (b) of FBK SiPM prototypes[22].

2.4.2 Noise sources

Despite the many advantages in the use of SiPMs, this kind of sensors can be affected by several source of noise, such as: the dark current (DC rate or DCR), due to thermal pair generation in the active volume; the optical cross talk between pixels due to secondary photons emission during the avalanche; the afterpulsing, due to trapped charge carriers, and the temperature dependence of the breakdown voltage, since V_{bd} increase with temperature linearly, changing the OV value.

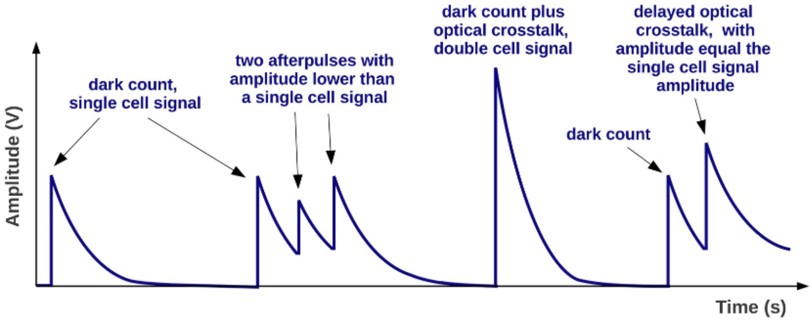

Figure 2.12: Analog SiPM output signal representation of all the different noise contributions[23].

The variations in the number of primary SPADs triggered by incoming photons (referred to as photoelectrons, N_{pe}) in an ideal photodetector are described by qN_{pe}. However, when accounting for non-ideal factors such as inter-SPAD cross-talk and integrated afterpulsing, which amplify the signal, the observed N_{pe} exceeds the true value. This discrepancy is commonly quantified by the excess charge factor (or noise factor) ECF $= \langle Q \rangle / \langle Q_N \rangle$, where $\langle Q \rangle$ represents the average total measured charge and $\langle Q_N \rangle$ is the average charge of the primary photoelectrons. This surplus charge manifests as an artificial gain, also termed the excess noise factor [24]:

$$ENF = \frac{(\sigma_Q / \langle Q \rangle)^2}{(\sigma_{Q_N} / \langle Q_N \rangle)^2} \tag{2.29}$$

where σ_Q denotes the standard deviation of the measured spectrum. Notice that afterpulsing and cross-talk are influenced by the intensity of the electric field, causing the ENF to rise with increasing OV.

2.4.3 NUV-HD technology

Near-UV High-Density (NUV-HD) technology [22], introduced in 2016 by Fondazione Bruno Kessler (FBK), can provide better electrical insulation thanks to deep trenches between microcells. Trenches are filled with silicon dioxide and they also provide partial optical insulation due to the different refractive index of the silicon. The active area is defined by a high energy ion implantation (called DI) which increases the electric field between the surface and DI, until avalanche. The space between DI and trenches, called virtual guard ring (VGR) region is not light-sensitive and prevents edge breakdown. The structure of a SiPM with NUV-HD technology is shown in Fig. 2.13.

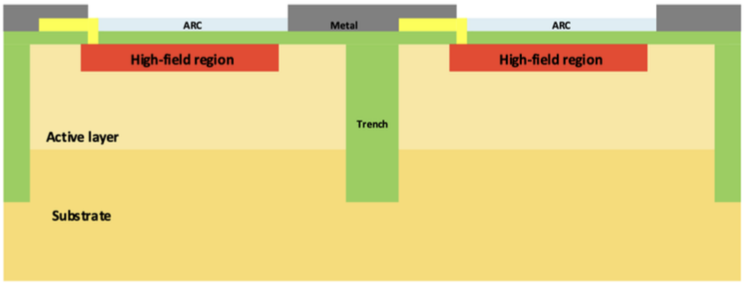

Figure 2.13: Scheme of the cells of the NUV-HD technology [22].

The spaces between DI and trench width are called critical dimensions (CDs) of the technology and minimized as much as possible in order to increase the sensor fill factor (FF), as previously defined in Eq. 2.28. where the active area is the area sensitive to the light, almost equal to the area of DI.

2.5 SiPMs for charged particles detection

SiPMs are usually coupled to scintillators for light-detection. However, recent studies have explored the possibility to detect charged particle with SiPMs [1, 2]. When a charged particle hits the sensor, the measured cross talk shows an excess with respect the standard CT-DC, i.e. the cross-talk measured on Dark Count events. In [2] it was shown that the effect was not related to an effect inside the silicon bulk, but to the presence of the protection layer where, at the passage of the charged particle, the Cherenkov effect produces a significant amount of photons; these photons, due to the small layer thickness, arrive on the SiPM surface with only few ps difference i.e. they are simultaneous on the SiPMs cells at the same time on the SiPM surface, generating a large signal with many firing SPADs.
This is suggested by the measurement of the CT fraction F_n, defined as the ratio between the number of firing SPADs and the total number of firing SPADs:

$$F_n = \frac{\text{events with n fired SPADs}}{\text{events with } \geq 1 \text{ fired SPADs}} \tag{2.30}$$

By repeating the measurement of F_n for different samples at different OV with the particle impinging from the front (resin protection layer) and from the back (no resin) of the sensors, it can be proved that if the beam comes from the side without protection layer the intrinsic CT is consistent with the measured CT, indicating a majority of 1

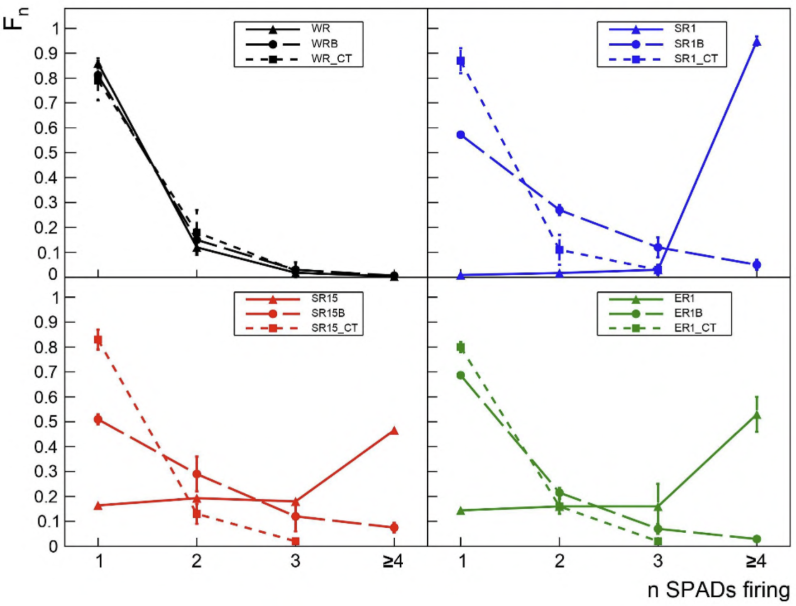

Figure 2.14: Measured CT factor F_n with respect to the number of fired SPADs for samples without resin (WR) and with silicone (SR) and epoxy (ER) resin. Square markers indicate intrinsic CT measured in the region before the signal, triangle markers indicate data with beam from the front of the sensor, circular markers indicate data with beam from the back of the sensor [2].

SPAD events. On the contrary, a multi-SPADs (≥ 4) signal is present if the particle hits the sensor from the side with a protection layer. The measurement of F_n is shown in Fig. 2.14.

The same series of studies proved that the time resolution improves as the number of hit SPADs increases, showing a scaling following $1/\sqrt{N_{SPAD}}$. Results from [2] are shown in Fig. 2.15

The occurrence of events involving a small number of SPADs is minimal. Utilizing such sensors for charged particle detection significantly enhances noise rejection compared to conventional photon detection. By setting a threshold of more than three SPADs, an efficiency exceeding 99% is achieved, effectively eliminating noise events caused by DCR and CT. Conversely, for the sensor without resin coverage (WR), the time resolution at thresholds of two or three SPADs is severely impacted by DCR and CT.

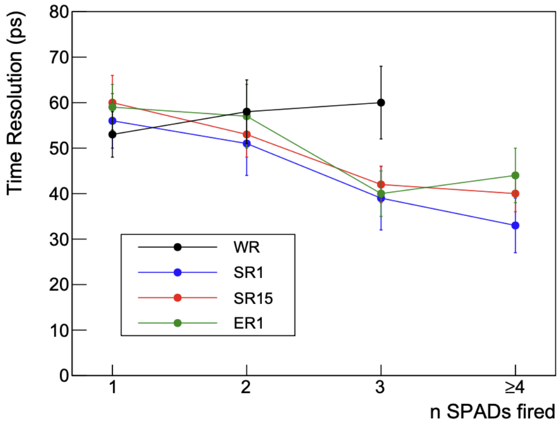

Figure 2.15: Time resolution as a function of the number of SPADs fired for the different SiPMs at an OV of ~ 6 V [2].

2.5.1 Recent developments in readout techniques

Among the new challenges in collecting the signal of a SiPMs there is the capability to read-out a matrix of SiPMs, i.e. to collect simultaneously the signal coming from a structure made by more SiPMs.

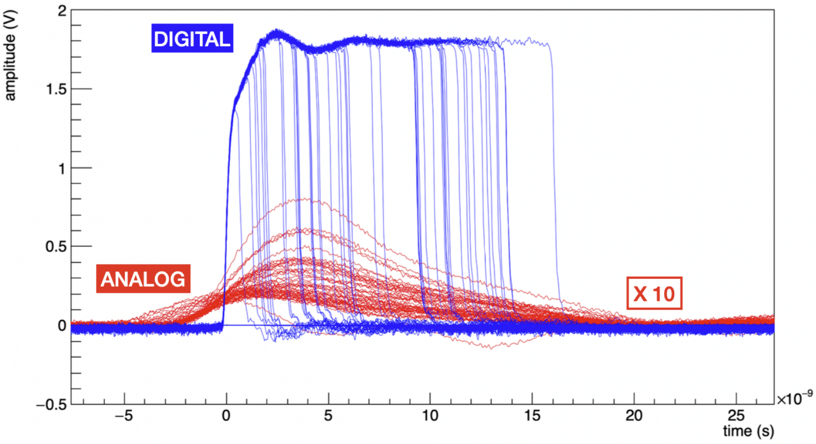

Figure 2.16: 50 triggers of analog (input in LIROC) to digital (output to pTDC) one SIPM of a matrix of 9 SIPMs with total area 3×3 mm^2, pixel pitch of 40 μm and 30 mV of threshold. The red curve is from the analog probe on the LIROC input (after amplification, before being discriminated) and the blue curve is the discriminated LIROC output signal. Here the LIROC has a gain of 14-15 dB and the red curve is shown with a factor ×10 to better understand the visualization.

The ALICE 3 group of INFN-Bologna started in 2024 a campaign to collect data from SiPMs [25] combining the possibility to read-out matrices and to cover the whole

Cherenkov cone formed in the protection during the passage of a charged particle. The setup, tested in few beam tests at CERN-PS, consists of the combination of the Weeroc LIROC ASIC chip [26] with an ultra fast (ps) Time to Digital Converter (picoTDC) developed at CERN [27]. The LIROC has 64 channels (56 to the picoTDC and 8 to the oscilloscope), each with an amplifier and a discriminator with the possibility to connect up to 64 SiPMs with the same V_{bias} and with a maximum readout of $\sim$ 200 MHz per channel. The PicoTDC works in double edge mode to retrieve the rising and falling hits timing and allow to collect the information of the Time Over Threshold (TOT) of the signals. The trigger of the pTDC is given by the signal of an LGAD placed as the first detector hit by the particles beam. This information is used in the analysis to be able to correct for time slewing. An example of an analog and a digital signals registered with this system for preliminary study is shown in Figure 2.16. Note that the sensors preliminary studied with this system differs with respect those considered in Chapter 3. therefore a direct comparison between the SiPMs signals under study in this work and the one collected with an analogue probe before being discriminated shown in Figure 2.6 is not possible.

Chapter 3

SiPM measurements

The following chapter provides a description of the SiPMs considered in this thesis studies and the results about their timing response. The sensors are standard SiPMs produced by FBK with different thickness of the protection resin layer 1×1 mm^2 active area. Preliminary studies on noise and IV were performed at INFN-Bologna laboratory. In this chapter their timing response before and after receiving a known dose of irradiation at TIFPA facility in Trento is evaluated. Their timing performances are compared by using data from a beam tests of November 2022 (before irradiation) and July 2023 (after irradiation), conducted at T10 beamline of CERN-PS.

3.1 Detectors under study

For this thesis studies, SiPMs produced by FBK were used, based on the NUV-HD-RH (Near UV - High Density - Radiation Hardness) technology [22]. On the basis of the protection layer thickness, two type of SiPMs were under study, whose features are reported in Table 3.1. Note that in this thesis work the two sensors considered are named SR1 and SR15, referring to the material of the protection layer (Silicone Resin) and its thickness (1 mm and 1.5 mm, respectively). Their performance have been previously studied in [2]. In this thesis they are studied after an irradiation at TIFPA of $10^{1}0$ and 10^{9} 1 MeV n$_{\mathrm{eq}}$ cm^{-2}, respectively.

			SPAD		**Protection layer**		
	Area (mm^2)	**FF (%)**	**Pitch**	**#**	**Type**	**Thick**	**RI**
SR1	1×1	72	20 µm	2444	Silicone	1.0 mm	1.50
SR15	1×1	72	20 µm	2444	Silicone	1.5 mm	1.50

RI = Refraction Index.

Table 3.1: Main features of the SiPMs under test.

Notice that the thickness of the protection layer is measured from the board (PCB) on which the sensor is hosted and, since the thickness of the sensor itself is 550 μm, this value must be subtracted from the value of the resin reported in Tab. 3.1. Thus, the effective protection layer is 450 μm for the 1 mm resin and 950 μm for the 1.5 mm one, as shown in Fig. 3.1.

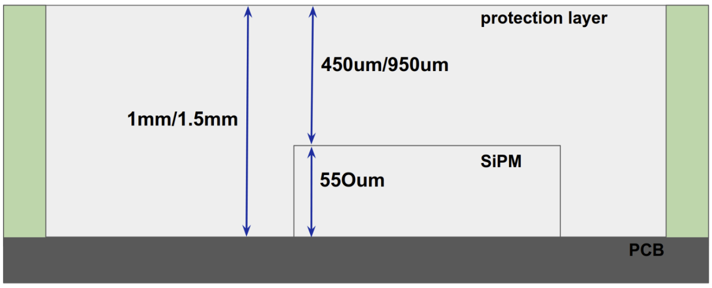

Figure 3.1: Scheme of the SiPM covered by a resin protection layer.

SR1 and SR15 sensors were previously studied in [1] as a part of a six SiPMs structure, while starting from November 2022 the protection layer was applied on a single SiPM with a precise area of 1.7×3.5 mm^2, covering also the wire bonding. A picture of the single SiPM structure is shown in Figure 3.2. This was done in order to better understand the Cherenkov effect inside the protection layer, as explained in [2].

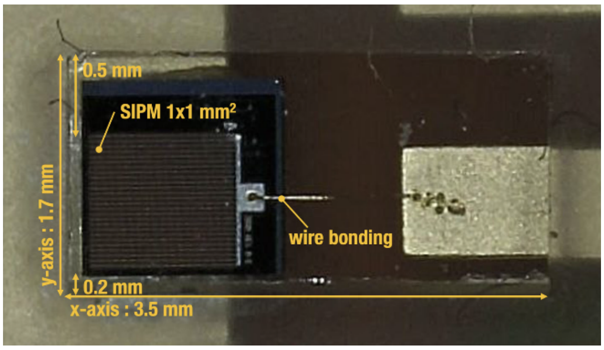

Figure 3.2: Single SiPM of 1×1 mm^2 active area covered by a protection layer of 1.7×3.5 mm^2, were the dimensions corresponds to the x and y coordinates respectively [2].

3.2 Preliminary measurements

3.2.1 IV curve

The IV (current-voltage) curve is a crucial step in characterizing a silicon detector operating under reverse bias, with the goal of determining the optimal operating voltage for the device. For SiPMs, the primary concern is identifying the transition to Geiger mode, where a self-sustained avalanche process begins. This occurs beyond a characteristic voltage known as the breakdown voltage V_{bd}. The instrumentation used includes a TDK Lambda Z100-2 power supply and a Keithley 6487 picoammeter. The circuit is configured so that the cathode of the sensor is biased with a positive voltage, while the anode is connected to the picoammeter to measure the current. The IV characteristics for the two sensors are shown in Figure 3.4.

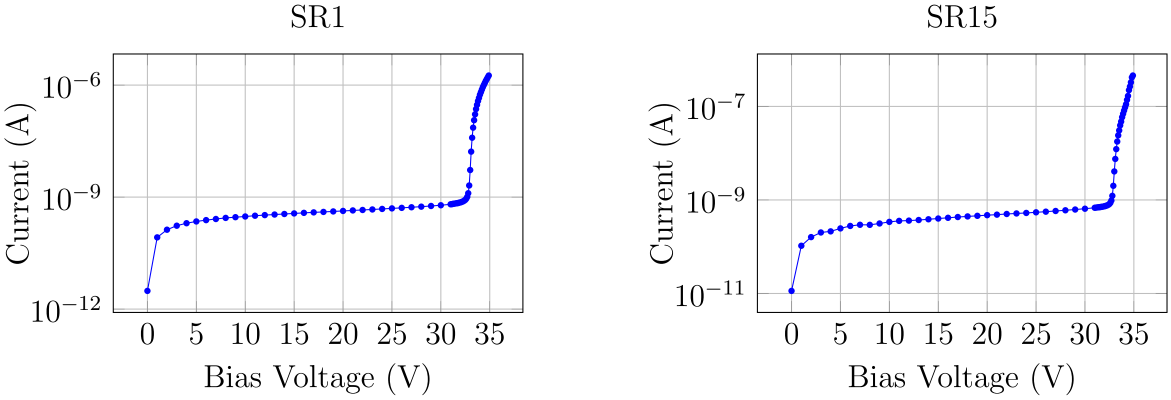

Figure 3.3: IV curves for the two sensors. The data was collected only until 35 V ($\sim$ 2 V OV) in order to focus on a more precise extraction of the V_{bd}, expected to be around 33 V.

The value of V_{bd} was extracted from a fit of the experimental data relying on two methods: the logarithmic derivative (LD) and the inverse logarithmic derivative (ILD) functions. The first method calculate the derivative of the logarithm of the IV curves defined as:

$$LD = \frac{\mathrm{d}ln(|I|)}{\mathrm{d}V} \tag{3.1}$$

The second case, its inverse function is considered:

$$ILD = \left(\frac{\mathrm{d}ln(|I|)}{\mathrm{d}V}\right)^{-1} \tag{3.2}$$

Below the breakdown voltage, LD shows a linear dependence on voltage with a positive slope. However, as it gest close V_{bd}, its behavior becomes quadratic, forming a parabolic shape with its vertex corresponding to the breakdown voltage. A similar trend is observed for ILD, but with an opposite slope: ILD reaches its minimum at V_{bd}, meaning that its inverse, LD, is at maximum. To determine V_{bd}, a parabolic fit is applied to both curves and the minimum is identified within a selected interval centered around the breakdown voltage. A schematic representation of the two methods is shown in Figure 3.4. In Table 3.2 the obtained results are reported.

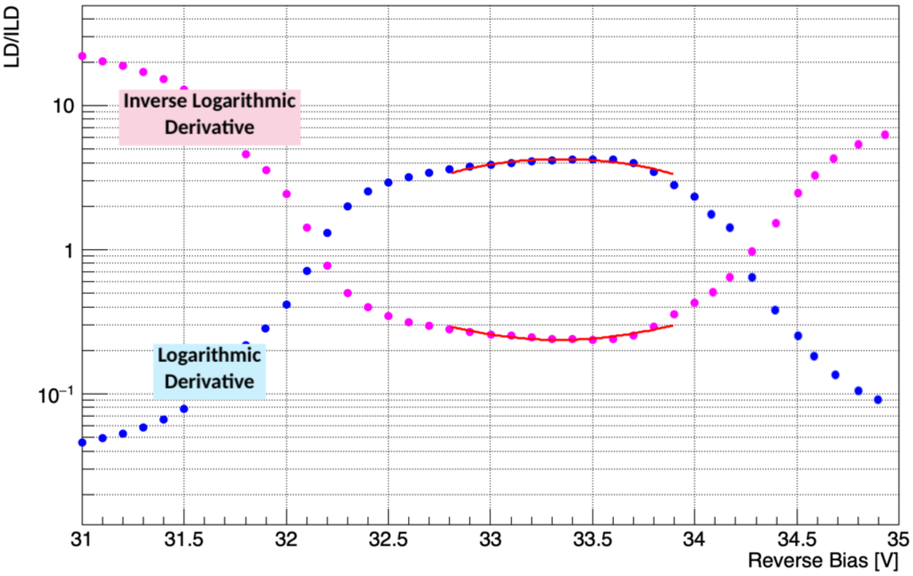

Figure 3.4: Schematic representation of the LD/ILD methods used to obtain the V_{bd}. The red curve represent the fit on the two curves.

sensor	V_{bd} (V)
SR1	33.4 ± 0.1
SR15	33.5 ± 0.1

Table 3.2: Breakdown voltages extracted with the LD/ILD method.

3.2.2 DCR

The Dark Count Rate, introduced in Section 2.4.2, is one of the main noise source of a SiPM. DCR is obtained by counting how many times the signal exceeds the value attributed to one SPAD hit in dark conditions. The DCR of the sensors was evaluated using the acquisition region of the oscilloscope in a time interval of 200 ns with an amplitude of 40 dB at room temperature, by acquiring the signal when the sensor is isolated from any photon source. The signal rate is then determined by counting how often it surpasses the threshold defined for one SPAD hit. Before any irradiation it was measured to be $\sim 6 \times 10^4$ Hz at 6 V_{OV} [15], in agreement with [28].

The results after irradiation are reported in figure 3.5 and 3.6 as a function of the applied threshold expressed in V. The DCR of irradiated sample is of the order of 10^6 Hz/mm^2, indicating a worsening with respect not irradiated sample, and it is reduced by one order of magnitude for a threshold of $\sim$ 1600% (SR1) and of $\sim$ 1000% (SR15) 1 SPAD at 6 V OV. In Table 3.3 the results at 50% of 1 SPAD.

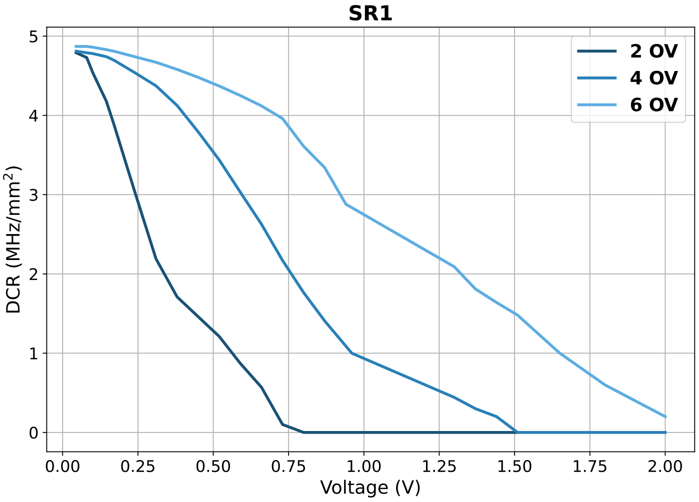

Figure 3.5: DCR versus threshold for SR1 at 2, 4 and 6 V OV after irradiation. The 100% of 1 SPAD corresponds to 0.075 V, 0.125 V and 0.175 V for 2, 4 ad 6 V OV respectively.

sensor OV	2V	4V	6V
SR1	4.73 MHz/mm^2	4.78 MHz/mm^2	4.87 MHz/mm^2
SR15	4.78 MHz/mm^2	4.82 MHz/mm^2	4.91 MHz/mm^2

Table 3.3: DCR measured at different OV at a threshold of 50% of 1 SPAD.

Note that the sensors were tested on the beam before being brought to TIFPA and the quoted irradiation is to be considered as a lower limit. Indeed, the accumulated radiation, which we estimate to be of the order of 10^9 1 MeV n_{eq} cm^{-2} in the previous beam tests, can be addressed as an indicative received dose before TIFPA irradiation.

3.3 SiPMs studies

3.3.1 Beam test setup

The investigation of SiPM response to charged particles was conducted at the T10 beamline of CERN-PS during two separate beam tests in November 2022 and July 2023.

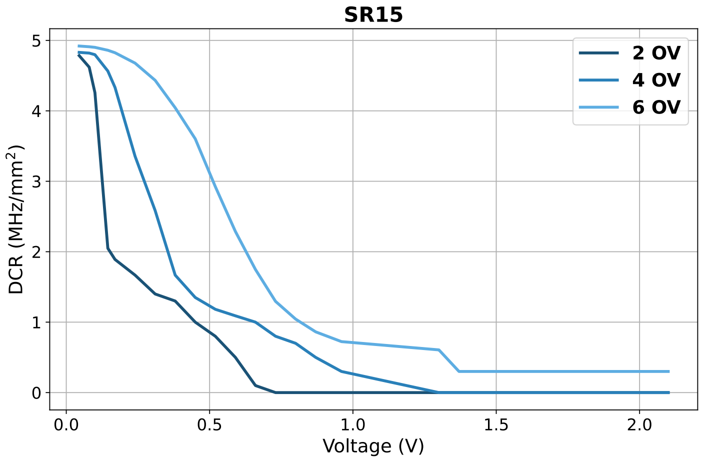

Figure 3.6: DCR versus threshold for SR15 at 2, 4 and 6 V OV after irradiation. The 100% of 1 SPAD corresponds to 0.075 V, 0.125 V and 0.175 V for 2, 4 ad 6 V OV respectively.

At an energy of 10 GeV/c, the positive beam primarily consisted of protons (80%) and pions (20%).

For the July beam test, the experimental setup, shown in Figure 3.7, included four sensors: two SiPMs under evaluation and two LGAD detectors (prototypes with a 1 × 1 mm^2 area and thicknesses of 35 μm or 25 μm) [12]. The LGADs served as triggers and as a timing reference (t_0), defining the active area of the beam. All equipment was remotely controlled from the control room using LabVIEW applications, which facilitated data transfer and storage, as well as regulation and monitoring of V_{bias}, currents, and box temperature. Furthermore, fast online analysis enabled real-time data verification.

Each SiPM signal was independently amplified with a gain factor of 40 dB using an XLEE amplifiers, corresponding to a voltage gain of 100 for signal frequencies ranging from 1 MHz to 1 GHz. Power was supplied to the SiPMs using TDK Lambda Z100 units, while the LGADs were powered by a CAEN N1470 4-channel high-voltage supply. A Lecroy WaveRunner 94904M-MS digital oscilloscope was used to record the waveforms, operating at a maximum bandwidth of 4 GHz. The trigger signal was generated by the coincidence of the two LGADs signals within the telescope. Since the oscilloscope captures complete signal waveforms, the digitization process was performed during data analysis.

Every sensor is mounted on an independent micro-positioner inside the setup box. These positioners allowed remote control of the positions of the SiPM and LGAD along the x and y axes with a precision of approximately 10 μm. Again, the positioners were operated remotely, in this case via an Arduino board, which was connected to the control

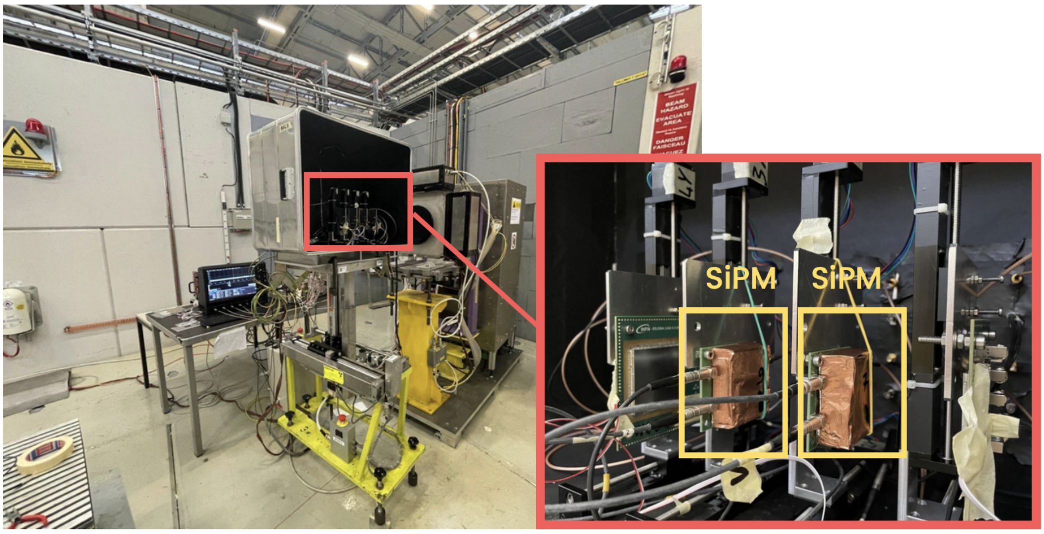

Figure 3.7: Experimental setup at T10-PS line at CERN during the test beam. The SiPMs are covered by copper boxes.

room and controlled through a LabVIEW program.

A schematic representation of the sensors assembled on the beam line with respect to the beam direction is shown in Figure 3.8.

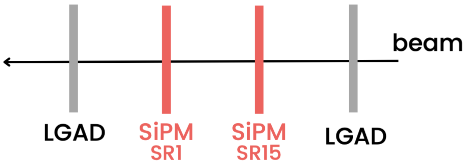

Figure 3.8: Position of the sensor in the telescope on the beam line.

3.3.2 Signal selection

Given the LGADs trigger condition time t_0, the signal events collected by the oscilloscope are those with a SiPM signal in a window of ± 2 ns from t_0. The DCR signals are those measured in the control region before the signal, between -6.5 ns and -2.5 ns from t_0. A first correction was made by subtracting the baseline from the signal, which was calculated on a time interval of 5 ns in the region before the rising edge. Figure 3.9 shows an example of baseline correction for SR15 at 2 V OV.

In addition, an example of a signal shape before and after irradiation with the baseline correction is shown in Figure 3.10. Notice that there are almost no difference among the two waveforms, apart from small alignment differences.

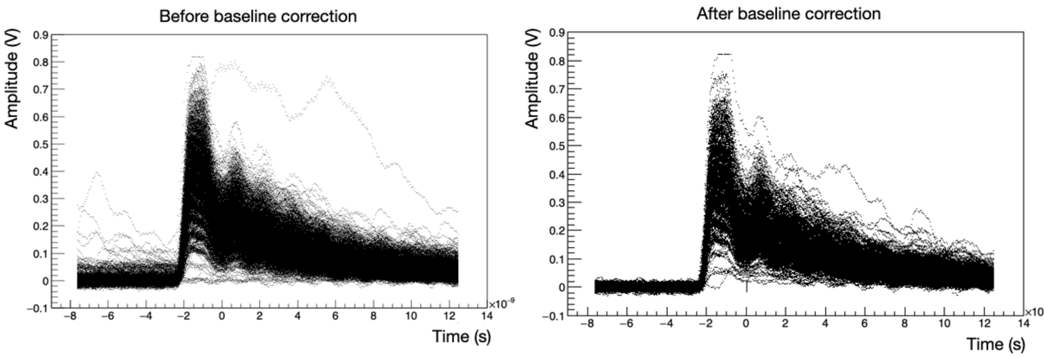

Figure 3.9: Signal of SR15 at 2V OV before and after baseline correction.

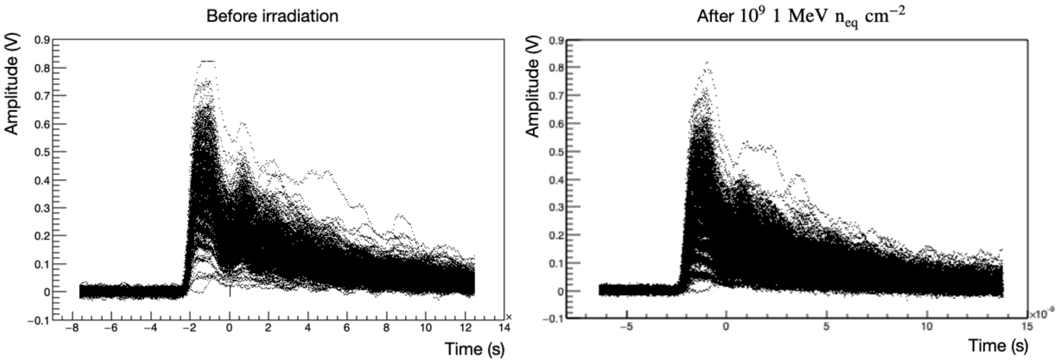

Figure 3.10: Signal of the sensor SR15 at 2V OV after offline selection of the SiPM waveforms, before (a) and after irradiation (b).

For the timing analysis, a fixed threshold of 50% (percentage referred to the amplitude of the first SPAD) of the single SPAD signal amplitude was used for the tested SiPMs, while a CFD (Constant Fraction Discrimination) threshold of 50% was used for the reference LGADs. This value for the SiPMs was chosen after evaluating the behavior of the time resolution as a function of the fixed threshold percentage for different numbers of firing SPADs. The results are shown in Figure 3.11 at an OV of 4 V. The values in Volts for the fixed threshold used was 0.03, 0.05 and 0.08 V for 2, 4 and 6 V OV respectively.

Figure 3.12 shows the amplitude of the signal, highlighting the discrimination between one SPAD and the other: the first peak corresponds to 1 SPAD firing, the second one to 2 SPADs firing and so on. The process to extract of the time resolution of the sensor as a function of the number of firing SPADs requires to apply proper cuts on the discriminated amplitude peaks, in correspondence to the different number of SPADs. By increasing the OV, the peaks corresponding to the single SPADs are reduced but it was still possible to distinguish them until 6 and 7 SPADs even at 6 V OV.

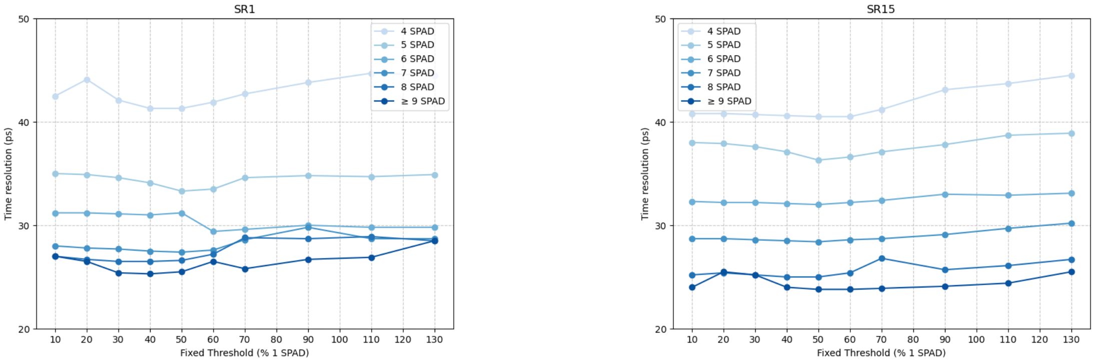

(a)

(b)

Figure 3.11: Time resolution as a function of the fixed threshold at different percentage, referred to the amplitude of the first SPAD at 4V OV for SR1 (a) and SR15 (b).

3.3.3 Time resolution before and after irradiation

For the timing analysis, the measurements were always performed using the LGAD as a reference. For the SiPM, the baseline value is evaluated event per event in the control region and subtracted from the signal; then, starting from the evaluated baseline, a threshold of 50% of 1 SPAD value was applied for the timing measurement. A CFD (Constant Fraction Discrimination) threshold of 50% was used for the reference LGADs. The time resolution of a SiPM is evaluated by using the time difference between the SiPM under test and the LGAD closest to the beam entrance. An example of the time difference distribution is shown in Figure 3.13.

The resolution σ_{fit} of the time difference distribution comes from a q-Gaussian fit. It is given by:

$$\sigma_{fit} = \sqrt{\sigma^2_{SiPM} + \sigma^2_{LGAD}} \tag{3.3}$$

where σ_{LGAD} is the intrinsic LGAD resolution, corresponding to $\simeq$ 27.1 ps (at 250 V) for the November 2022 teat beam and to $\simeq$ 31.2 ps (at 110 V) for July 2023 data [12].

The time resolution of the sensors was studied as a function of the number of SPADs firing in the SiPM for different values of overvoltage: 2, 4 and 6 V OV. Figures 3.14 - 3.19 compares the time resolution versus the number of fired SPADs before and after irradiation at different OV. Notice that the the time resolution is provided starting from 2 or 4 SPADs since ratio between counts for that SPAD and total SiPM selected events, was found to be larger than 95% for more than 4 fired SPADs and larger than 98% for more than 2 fired SPADs for all the OV. The last nSPAD reported on the horizontal

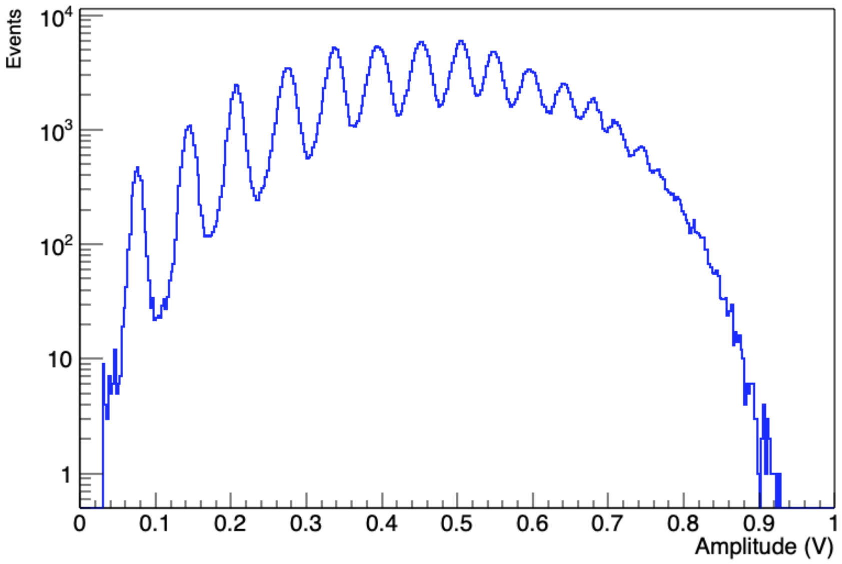

(a)

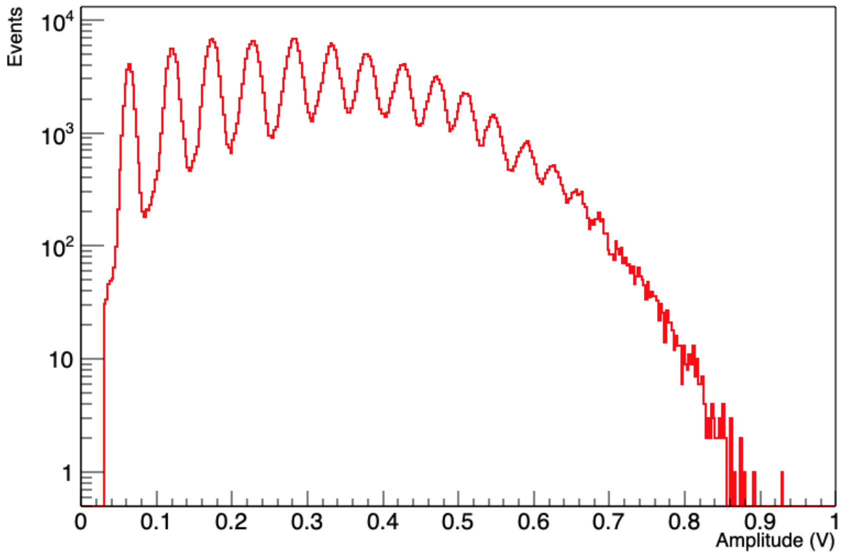

(b)

Figure 3.12: Signal amplitude from SR1 (a) and SR15 (b) at 2 V OV. The first peak related to the small inefficiency of the signal was cut from the visualization.

axis refers to all the events for a number equal or greater of firing SPADs, which were not always possible to clearly distinguish anymore after a SPADs. Moreover, an additional horizontal is set above the plots to indicate the signal amplitude of the signal corresponding to the single SPADs (cfr. Figure 3.12). All the points are shown with a 10% error.

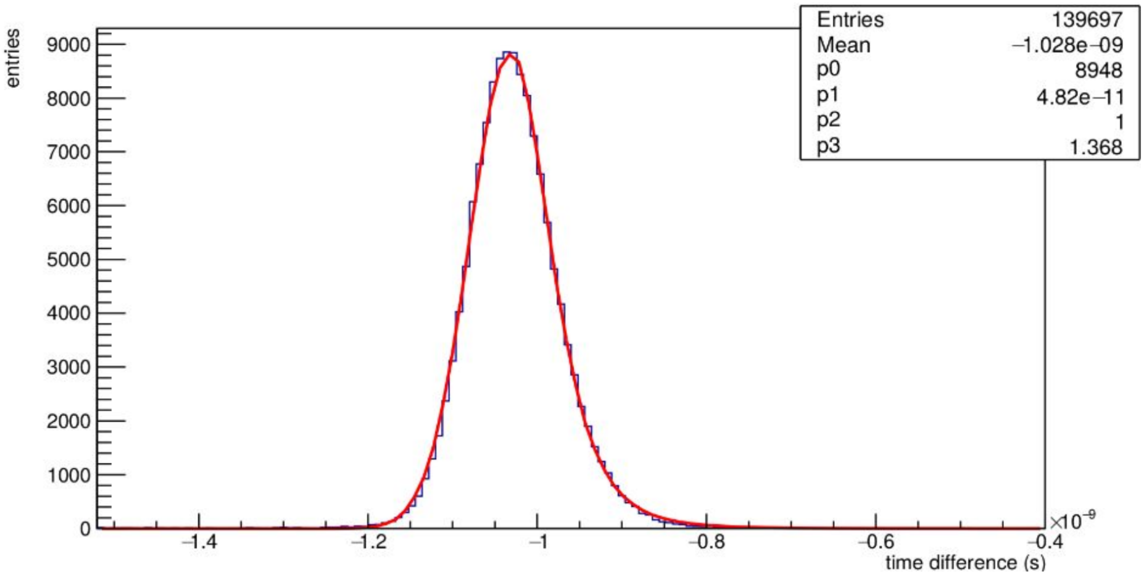

Figure 3.13: Example of time difference between the SiPM and the trigger LGAD for events with ≥ 4 SPADs. The parameter p_1 represents the σ_{fit}.

It can be seen that the performance of the SiPMs is not degraded at 2V OV while it is marginally worsened at 4 and 6V OV. At 2 and 4 V OV (Figures 3.14-3.17) the time resolution at 4 SPADs sets around 40-45 ps and it decreases until 20-25 ps when more than 9 SPADs are fired. Notice that the results of SR15 at 4 V OV seems to be not compatible within the error with respect before irradiation, but the time resolution of $\sim$ 23 ps for more than 9 firing SPADs confirms an excellent response of the sensor even after irradiation. At 6 V OV (Figures 3.18-3.19)it was possible to extract the time resolution until 6 or 7 SPADs due to the intrinsic functioning of the SiPM response. In this case the time resolution is shown starting from 2 firing SPADs (around 70-75 ps) and even in this case the resolution improved until 25-35 ps.

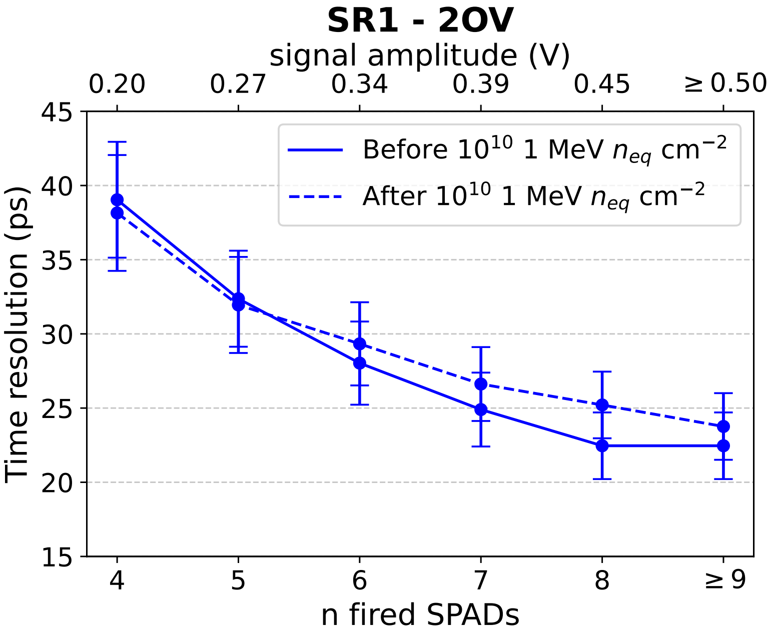

Figure 3.14: Time resolution of SR1 sensor as a function of the number of fired SPADs at 2 V OV.

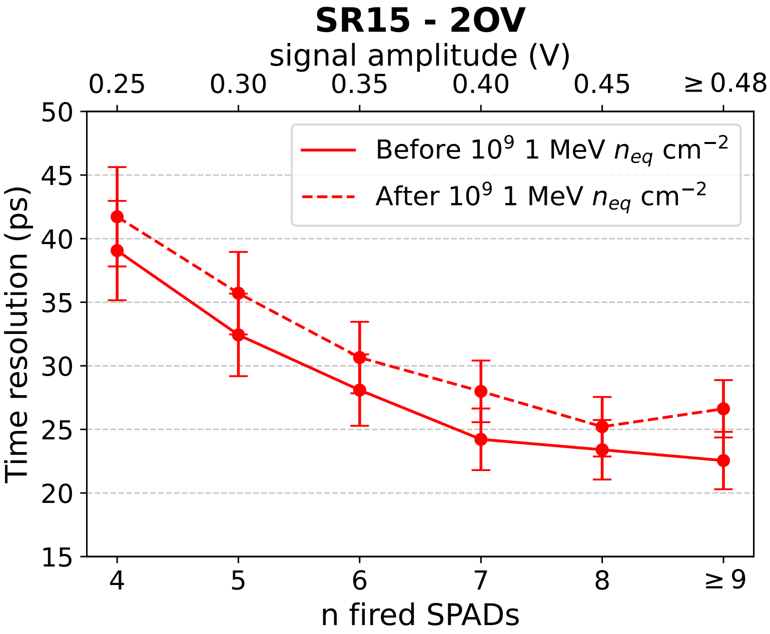

Figure 3.15: Time resolution of SR15 sensor as a function of the number of fired SPADs at 2 V OV.

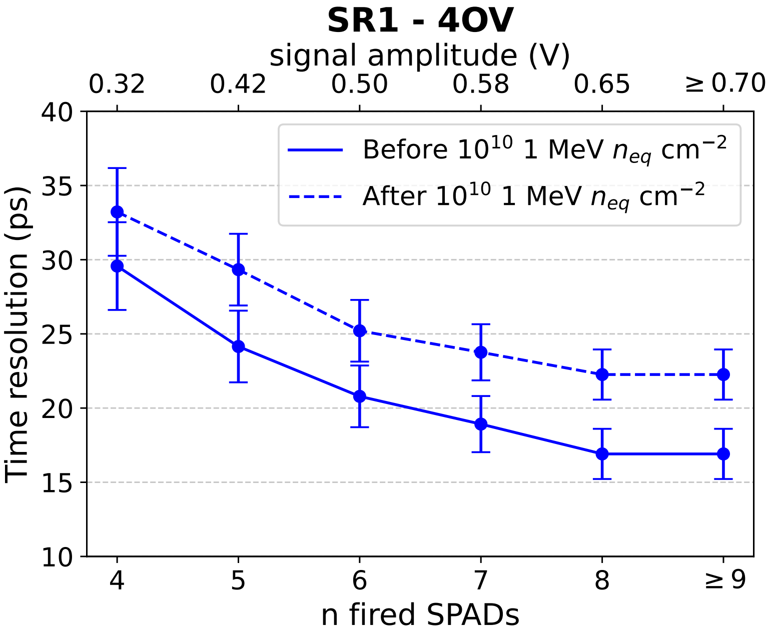

Figure 3.16: Time resolution of SR1 sensor as a function of the number of fired SPADs at 4 V OV.

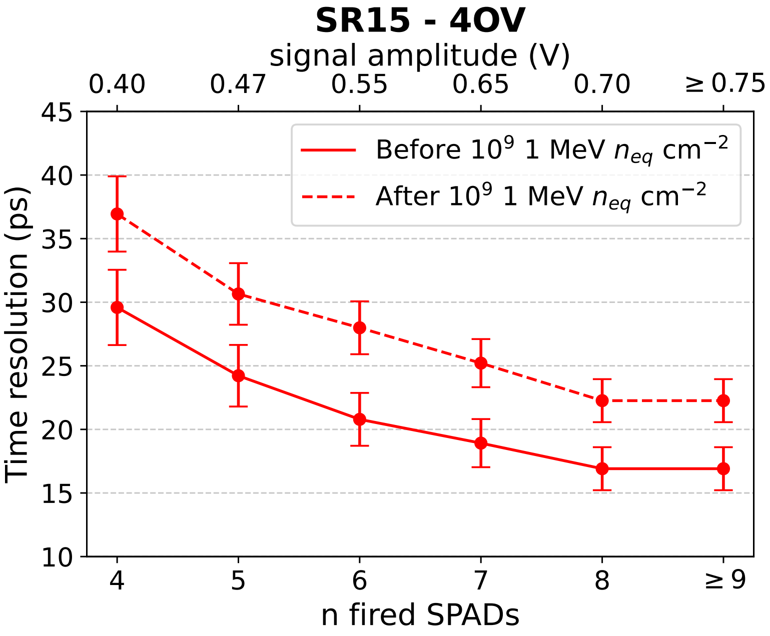

Figure 3.17: Time resolution of SR15 sensor as a function of the number of fired SPADs at 4 V OV.

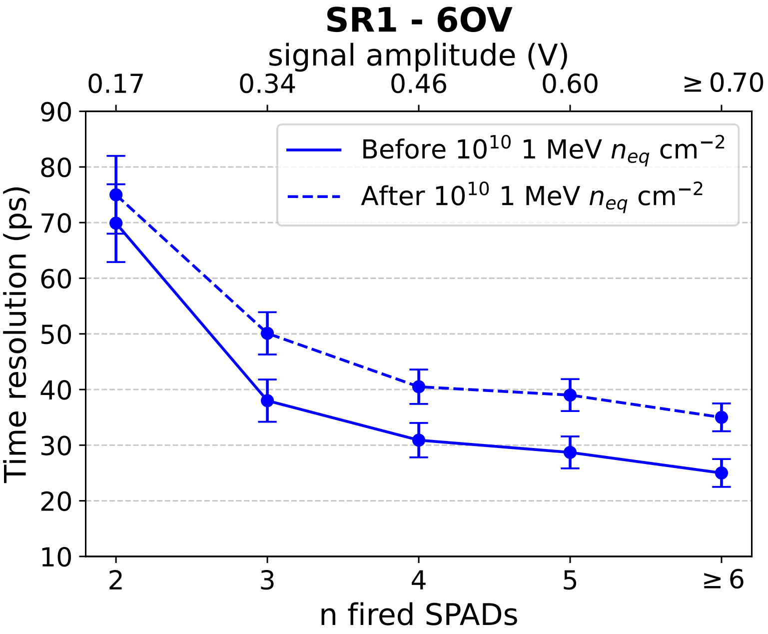

Figure 3.18: Time resolution of SR1 sensor as a function of the number of fired SPADs at 6 V OV.

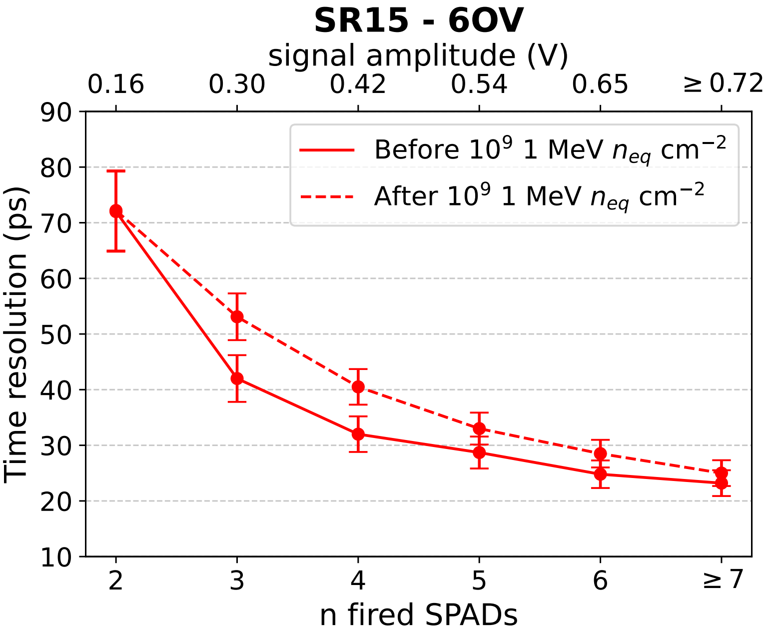

Figure 3.19: Time resolution of SR15 sensor as a function of the number of fired SPADs at 6 V OV.

Conclusions

In this thesis, the performances of SiPM devices before and after the irradiation with known dose of non ionizing radiation have been studied. The SiPMs were tested in different beam tests at the CERN-PS T10 beamline, one in November 2022 and one in July 2023 within a series of beam test campaigns led by the ALICE group of INFN-Bologna. The two sensors considered in this work were NUV-HD-RH SiPM, produced by FBK, with a sensitive area 1×1 mm^2, pixel pitch of 20 μm and a silicone resin protection layer of 1.0 and 1.5 mm.

A first study of the measurements of the 2022 beam test was reported in [2, 15], showing the origin of the multi-SPAD signal: this has been found to be associated to cherenkov light emission in the protection layer on top of the SIPM.. This produce many SPADs firing at the same time on the device resulting in very high efficiencies, with the majority of events with more than 4 SPADs firing. The extraction of time resolution was carried out also in this thesis work alongside the study of the 2023 beam test data. Since the sensors were tested on the beam before being brought to TIFPA and the quoted irradiation is to be considered as a lower limit. The doses of 10^{10} and 10^{9} MeV $\mathrm{n_{eq}}$ cm^{-2} for SR1 and SR15 were chosen in order to evaluate possible differences between the samples aafter different levels of radiation.

After being exposed by radiation the two sensors were characterized again, confirming a breakdown voltage V_{bd} of around 33.5 V. The time resolution as a function of the number of firing SPADs was extracted from the data of the beam tests, and a comparison before and after 10^{10} MeV $\mathrm{n_{eq}}$ cm^{-2} was shown for different values of overvoltage: 2, 4 and 6 V. The results at 2 V OV are compatible while at 4 and 6 V OV the time resolution seems marginally degraded. At 2 V and 4 V OV, the time resolution with 4 SPADs stabilizes around 40-45 ps and gradually decreases to 20-25 ps when more than 9 SPADs are activated. It is worth noting that the SR15 results at 4 V OV indicate a time resolution of approximately 23 ps for more than 9 triggered SPADs confirms the sensor's outstanding performance even after irradiation. At 6 V OV, the time resolution could be determined only up to 6 or 7 SPADs due to the intrinsic characteristics of the SiPM response. In this scenario, the resolution starts from around 70-75 ps with 2 active SPADs and improves to 25-35 ps as more SPADs are involved. Even if in some cases the time resolution after the irradiation was not exactly compatible within the error with respect to the resolution before, the two sensors demonstrate the capability to keep a resolution up to 20-25 ps, confirming the possibility to be considered as candidate for different physics applications. The DCR of the sensors show a worsening of two orders of magnitude with respect the one calculated before being irradiated, in agreement of what expected for an irradiated sensor. In particular it was found to be of the order of few MHz/mm^2 with the possibility to get reduced by at least one order of magnitude after applying an appropriate threshold. For 6 (SR1) and 7 (SR15) firing SPADs, corresponding to the best time resolution achieved, the DCR is still $\sim$ 3.9 MHz/mm^2 (SR1) and $\sim$ 1.2 MHz/mm^2 (SR15). Further studies with irradiated sensors or new technologies (BSI) will establish the possible limits of this technique in harsh environments.

Bibliography

[1] F Carnesecchi et al. “Direct detection of charged particles with SiPMs”. In: *Journal of Instrumentation* 17.06 (2022), P06007.

[2] F Carnesecchi et al. “Measurements of the Cherenkov effect in direct detection of charged particles with SiPMs”. In: *The European Physical Journal Plus* 138.9 (2023), p. 788.

[3] *LHC long term schedule.* 2023. URL: `https://lhc-commissioning.web.cern.ch/schedule/LHC-long-term.htm`.

[4] ALICE collaboration et al. “The ALICE experiment-A journey through QCD”. In: *arXiv preprint arXiv:2211.04384* (2022).

[5] Matteo Cacciari et al. “Theoretical predictions for charm and bottom production at the LHC”. In: *Journal of High Energy Physics* 2012.10 (2012), pp. 1–24.

[6] ALICE collaboration et al. “Letter of intent for ALICE 3: A next-generation heavy-ion experiment at the LHC”. In: *arXiv preprint arXiv:2211.02491* (2022).

[7] Frithjof Karsch. “Quark deconfinement and J/psi suppression in heavy ion collisions”. In: *Part. World* 1 (1989), pp. 24–26.

[8] Vyacheslav Lysov, Sabrina Pasterski, and Andrew Strominger. “Low’s subleading soft theorem as a symmetry of QED”. In: *Physical Review Letters* 113.11 (2014), p. 111601.

[9] Walter Snoeys et al. “A process modification for CMOS monolithic active pixel sensors for enhanced depletion, timing performance and radiation tolerance”. In: *Nuclear Instruments and Methods in Physics Research Section A: Accelerators, Spectrometers, Detectors and Associated Equipment* 871 (2017), pp. 90–96.

[10] MP Casado, ATLAS HGTD Group, et al. “A high-granularity timing detector for the ATLAS phase-II upgrade”. In: *Nuclear Instruments and Methods in Physics Research Section A: Accelerators, Spectrometers, Detectors and Associated Equipment* 1032 (2022), p. 166628.

[11] Collaboration Cms. *A MIP timing detector for the CMS phase-2 upgrade.* Tech. rep. 2019.

[12] F. Carnesecchi et al. “Beam test results of 25 μm and 35 μm thick FBK ultra fast silicon detectors”. In: *The European Physical Journal Plus* 138.99 (2023). DOI: `10.1140/epjp/s13360-022-03619-1`.

[13] Nicola Nicassio et al. “A combined SiPM-based TOF+ RICH detector for future high-energy physics experiments”. In: *2023 9th International Workshop on Advances in Sensors and Interfaces (IWASI)*. IEEE. 2023, pp. 199–204.

[14] MN Mazziotta et al. “Development of a novel compact and fast SiPM-based RICH detector for the future ALICE 3 PID system at LHC”. In: *Journal of Instrumentation* 20.01 (2025), p. C01001.

[15] Bianca Sabiu. “Study of the timing response of SiPM in direct detection of charged particles for the TOF System of ALICE 3”. In: (2023).

[16] Martin A Green. “Self-consistent optical parameters of intrinsic silicon at 300 K including temperature coefficients”. In: *Solar Energy Materials and Solar Cells* 92.11 (2008), pp. 1305–1310.

[17] Ger de Graaf and Reinoud F Wolffenbuttel. “Illumination source identification using a CMOS optical microsystem”. In: *IEEE Transactions on Instrumentation and Measurement* 53.2 (2004), pp. 238–242.

[18] Francesca Carnesecchi. “Experimental study of the time resolution for particle detectors based on MRPC, SiPM and UFSD technologies”. In: (2018).

[19] Zhong He. “Review of the Shockley–Ramo theorem and its application in semiconductor gamma-ray detectors”. In: *Nuclear Instruments and Methods in Physics Research Section A: Accelerators, Spectrometers, Detectors and Associated Equipment* 463.1-2 (2001), pp. 250–267.

[20] Stefan Gundacker and Arjan Heering. “The silicon photomultiplier: fundamentals and applications of a modern solid-state photon detector”. In: *Physics in Medicine & Biology* 65.17 (2020), 17TR01.

[21] M Grodzicka-Kobylka, M Moszyński, and T Szcześniak. “Silicon photomultipliers in gamma spectroscopy with scintillators”. In: *Nuclear Instruments and Methods in Physics Research Section A: Accelerators, Spectrometers, Detectors and Associated Equipment* 926 (2019), pp. 129–147.

[22] Alberto Gola et al. “NUV-sensitive silicon photomultiplier technologies developed at Fondazione Bruno Kessler”. In: *Sensors* 19.2 (2019), p. 308.

[23] Fabio Acerbi and Stefan Gundacker. “Understanding and simulating SiPMs”. In: *Nuclear Instruments and Methods in Physics Research Section A: Accelerators, Spectrometers, Detectors and Associated Equipment* 926 (2019), pp. 16–35.

[24] Robert Klanner. “Characterisation of sipms”. In: *Nuclear Instruments and Methods in Physics Research Section A: Accelerators, Spectrometers, Detectors and Associated Equipment* 926 (2019), pp. 36–56.

[25] Davide Falchieri et al. “Design, test and performance of a PicoTDC based board”. In: *Journal of Instrumentation* 20.01 (2025), p. C01014.

[26] *Weeroc LIROC*. URL: `https://www.weeroc.com/read_out_chips/liroc/`.

[27] *picoTDC*. URL: `https://kt.cern/technologies/picotdc`.

[28] F. Acerbi et al. “Radiation damage effects of protons and X-rays on silicon photomultipliers”. In: *Nuclear Instruments and Methods in Physics Research Section A* 1047 (February 2023). DOI: `10.1016/j.nima.2022.167791`.